RESEARCH ARTICLE SUMMARY

NEUROIMMUNOLOGY

A chemogenetic screen reveals that Trpv1-expressing neurons control regulatory T cells in the gut

Yangyang Zhu†, Kimberly A. Meerschaert†, Silvia Galvan-Pena, Na-Ryum Bin, Daping Yang, Himanish Basu, Ryo Kawamoto, Amre Shalaby, Stephen D. Liberles, Diane Mathis, Christophe Benoist*‡, Isaac M. Chiu*‡

INTRODUCTION: The gastrointestinal (GI) tract is a complex sensory organ that integrates neuronal, epithelial, microbial, and immunological signaling. Within this framework, the interactions between the enteric nervous system (ENS), extrinsic sensory and autonomic ganglia, and gut-resident immunocytes maintain gut physiology at homeostasis and coordinate barrier defenses against pathogens. Dysregulation of neuroimmune cross-talk could underlie major GI disorders such as food allergies, chronic visceral pain, and inflammatory bowel diseases.

RATIONALE: Despite notable advances, the interactions through which the gut nervous and immune systems influence each other remains poorly understood. This is in part because of the limitations in manipulating these interactions in vivo and because the diversity of neuronal classes and immunologic cell types that are present within the gut gives rise to many potential cellular interactions. Chemogenetics provides the means to control the activity of specific neuronal cell types through DREADDs (designer receptors exclusively activated by designer drugs). For example, neuronal expression of hM3Dq, an activating DREADD, allows neuronal activation by administration of its ligand clozapine *N*-oxide (CNO). We applied a chemogenetic screen to dissect and map the interactions between neural and immunologic components in the gut.

RESULTS: We used eight different neuronal Cre mouse lines in combination with neonatal administration of the Cre-dependent AAV.PhP.S-DIO-hM3Dq virus to selectively target distinct vagal, dorsal root ganglia (DRG), and enteric neuron subsets. After activating neurons by administering CNO to these mice, we performed broad immunophenotyping of ileum, cecal, and colonic gut tissues by flow cytometry. Our analysis revealed distinct changes of immunocyte populations after neuronal activation. Nitrergic neurons, which are marked by Nos1 expression, regulated T helper 17 (T_H17)–like cells. Cholinergic neurons, which express ChAT, regulated neutrophils. Activation of Trpv1-expressing ($Trpv1^+$) nociceptive neurons had the broadest effects, resulting in down-regulation of myeloid populations and regulatory T (T_{reg}) cells that express the transcription factor RORγ in the colon. $Trpv1^+$ neuron activation induced distinctive transcriptional changes in T_{reg} cells and dampened their proliferation. Neuroanatomically focused activation and ablation approaches of distinct neurons revealed that $Trpv1^+$ neurons in the DRG, but not in the vagal ganglia, mediated this T_{reg} phenotype. Using genetically deficient mice, we found that the neuropeptide calcitonin gene–related peptide (CGRP) and its receptor RAMP1 were required for this neuroimmune interaction.

CONCLUSION: This work provides a framework to reveal functional neuroimmune interactions in the gut. Through an unbiased chemogenetic screen, we defined several intriguing, and previously unappreciated, neuroimmune interactions in the gut, including a role for $TRPV1^+$ nociceptors in controlling T_{reg} cell populations. Given the role of $Trpv1^+$ DRG neurons in pain signaling, and T_{reg} cells in controlling inflammatory responses, our findings suggest that pain signaling may be counterpoised with immunomodulatory mechanisms in the gut. In addition, the data provide a resource for neuroscientists, immunologists, and gastroenterologists who study cellular interactions in the gastrointestinal tract. ■

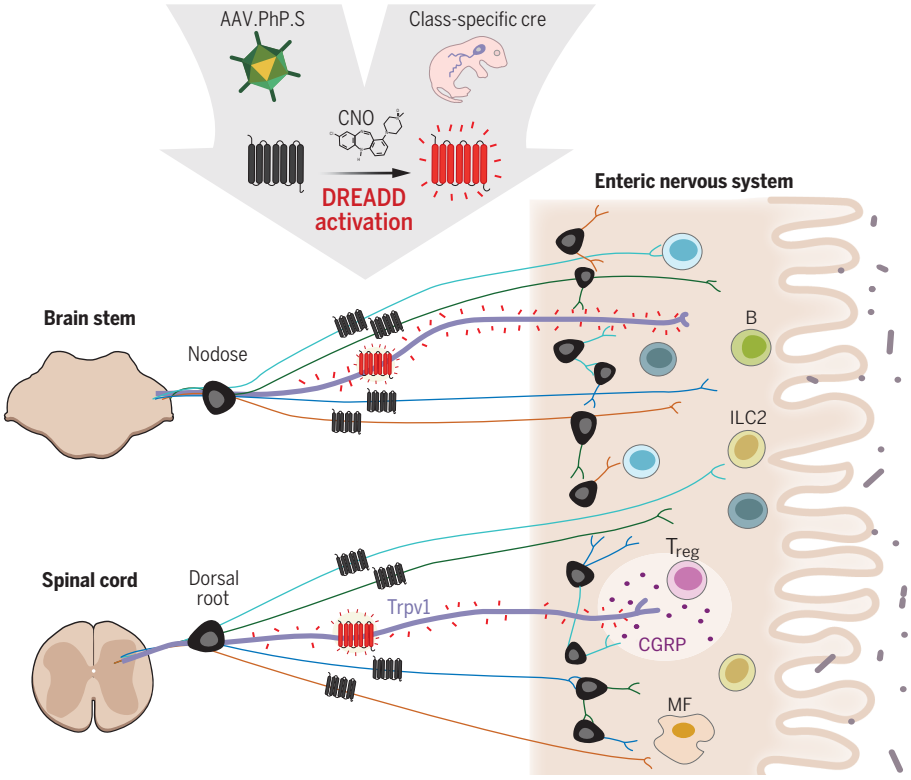

Nociceptor communication with intestinal immunocytes identified by chemogenetics. After delivery by a neuron-specific viral vector (AAV.PhP.S), DREADD expression was unleashed by Cre recombinase expressed in specific neuronal subtypes, which was later activated by administration of the CNO ligand. Activation of specific neurons induced homeostatic and phenotypic changes in the immunocyte populations with which they interact. Activation of $Trpv1^+$ spinal afferent neurons decreased gut T_{reg} cells and, in particular, the microbe reactive $ROR\gamma^+$ subset, via CGRP-RAMP1. B, B cell; ILC2, type 2 innate-like lymphocyte; MF, macrophage.

The list of author affiliations is available in the full article online.
*Corresponding author. Email: cb@hms.harvard.edu (C.B.); isaac_chiu@hms.harvard.edu (I.M.C.)
†These authors contributed equally to this work.
‡These authors contributed equally to this work.
Cite this article as Y. Zhu *et al.*, *Science* **385**, eadk1679 (2024). DOI: 10.1126/science.adk1679

READ THE FULL ARTICLE AT
https://doi.org/10.1126/science.adk1679

RESEARCH ARTICLE

NEUROIMMUNOLOGY

A chemogenetic screen reveals that Trpv1-expressing neurons control regulatory T cells in the gut

Yangyang Zhu[1]†, Kimberly A. Meerschaert[1]†, Silvia Galvan-Pena[1], Na-Ryum Bin[2], Daping Yang[1], Himanish Basu[1], Ryo Kawamoto[1], Amre Shalaby[1], Stephen D. Liberles[2], Diane Mathis[1], Christophe Benoist[1]*‡, Isaac M. Chiu[1]*‡

Neuroimmune cross-talk participates in intestinal tissue homeostasis and host defense. However, the matrix of interactions between arrays of molecularly defined neuron subsets and of immunocyte lineages remains unclear. We used a chemogenetic approach to activate eight distinct neuronal subsets, assessing effects by deep immunophenotyping, microbiome profiling, and immunocyte transcriptomics in intestinal organs. Distinct immune perturbations followed neuronal activation: Nitrergic neurons regulated T helper 17 (T_H17)–like cells, and cholinergic neurons regulated neutrophils. Nociceptor neurons, expressing Trpv1, elicited the broadest immunomodulation, inducing changes in innate lymphocytes, macrophages, and RORγ^+ regulatory T (T_{reg}) cells. Neuroanatomical, genetic, and pharmacological follow-up showed that Trpv1$^+$ neurons in dorsal root ganglia decreased T_{reg} cell numbers via the neuropeptide calcitonin gene–related peptide (CGRP). Given the role of these neurons in nociception, these data potentially link pain signaling with gut T_{reg} cell function.

The mammalian gastrointestinal (GI) tract is one of the body's critical barrier sites, interfacing for information exchange between the host, nutrients, and resident microbiota. A dynamic interplay between the immune system, nervous system, and microbial ecosystem maintains normal gut physiology and tissue integrity (*1*–*3*). The immune and nervous systems both possess exquisitely specific sensing and effector capabilities, and there is great interest in how they can be combined to sense chemical, damaging, or infectious threats at the GI frontier.

The GI tract is densely innervated by a complex network of sensory and autonomic neurons. Gut-innervating neurons include the enteric nervous system (ENS), a largely autonomous intrinsic system that coordinates motility and secretion. In addition, extrinsic sensory neurons from the dorsal root ganglia (DRG) and nodose ganglia (NG), as well as autonomic neurons that reside in the brainstem and sympathetic ganglia, project to the gut, modulating the activity of the ENS (*4*–*6*). DRG and NG neurons function primarily as sensory neurons, possessing multiple receptors such as Piezo2, transient receptor potential (TRP) channels, and G protein–coupled receptors (GPCRs) to detect mechanical stretch, dietary, and noxious stimuli. Gut-innervating neuronal populations are highly diverse, with many molecular categories identified by single-cell RNA sequencing (scRNA-seq) (*7*–*9*). The gut immune system is equally complex, with a representation of immunocytes from all lineages: cells expressing innate receptors that respond immediately to microbial patterns [macrophages or innate-like lymphocytes (ILCs)], adaptive T or B lymphocytes with tailored responses to antigens on microorganisms and food, and cell populations whose final role is to dampen inflammation and promote peaceful coexistence with symbiotic microbiota while ensuring barrier integrity and tissue repair [regulatory T (T_{reg}) cells, dendritic cells].

Several elegant studies in this field have targeted specific neuronal or immunologic subtypes and revealed specific neuroimmune interactions. For example, neurons expressing vasoactive intestinal peptide (VIP) have been shown to modulate the activity of ILC3s (*10*–*12*), and neuromedin U (NMU)–expressing enteric neurons amplify ILC2-driven type 2 immune responses (*13*–*15*). Sympathetic neurons mediate gut tissue protection by cross-talk with enteric macrophages (*16*, *17*) and ILCs (*18*). However, beyond these one-to-one interactions, there is a need for a more systematic and integrated approach to identify specific neuroimmune interactions in the gut.

Chemogenetic approaches (*19*) offer the potential for activation or inhibition of molecularly defined neurons and permit one to probe many such neuronal types in parallel. They rest on the targeted expression of DREADDs (designer receptors exclusively activated by designer drugs), which are engineered GPCRs that are inert except when activated by a synthetic ligand that has no counterpart or receptor in mammalian organisms. Neurons can thus be activated in a temporally controlled manner. If expressed as cell type–specific transgenes or delivered by viral vectors with fine tropism, they also allow spatial and anatomical targeting. For example, chemogenetics has allowed the identification of the neural basis of feeding and other behaviors (*20*, *21*).

In this work, we leveraged an intersectional chemogenetic approach to determine how distinct neurons modulate the gut immune system. DREADDs were expressed specifically to target the major classes of neuronal types that innervate the gut. Chemogenetic activation led to discrete alterations in immunocytes, especially for Trpv1$^+$ neurons.

Results

Neuron class–specific expression of chemogenetic effectors

We set up a systematic screen based on targeted expression of DREADD molecules to detect how activation of peripheral neuronal subtypes modulates the immune system and gut microbiome. Our overall strategy was to transduce, via an adeno-associated virus (AAV) vector, the DREADD-encoding sequence in an inactive configuration, which was unblocked by Cre recombinase expressed in specific neuronal subtypes, and finally activate these targeted neurons by injection of DREADD ligand (Fig. 1A). For expression, we used the AAV.PHP.S viral vector, which efficiently infects peripheral sensory and autonomic neurons in mice without boosting strong immune responses (*22*). It allows expression of a DREADD and a mCherry fluorescent protein under the human *SYN1* promoter, but only after inversion by Cre recombinase. As a DREADD, we used hM3Dq, a muscarinic Gq protein–coupled receptor that had been engineered to respond to the synthetic ligand clozapine *N*-oxide (CNO), leading to calcium influx and neuronal activation (*23*). CNO has a half-life of several hours in vivo, such that the neuronal activation was expected to last for several hours. High-titer AAV.PhP.S-hSyn-DIO-hM3Dq-mCherry stocks were injected into neonatal mice, an age that results in higher levels of neuronal labeling compared with adult injections and avoids immunologic confounders from recent viral infection (*24*).

For neuronal targeting, we chose a panel of eight transgenic mouse lines expressing Cre in major subsets of peripheral sensory and autonomic neurons that innervate the gut (data S1). From published scRNA-seq datasets (fig. S1A) and well-defined classical markers of gut innervating neurons (*25*, *26*), we chose the following driver genes: *Chat*, *Nos1*, *Vip*, *Tac1*, *Trpv1*, *Mrgprd*, *Th*, and *Piezo2*. These Cre lines (*27*–*34*) were chosen to label intrinsic neurons

[1]Department of Immunology, Blavatnik Institute, Harvard Medical School, Boston, MA 02115, USA. [2]Howard Hughes Medical Institute, Department of Cell Biology, Harvard Medical School, Boston, MA 02115, USA.
*Corresponding author. Email: cb@hms.harvard.edu (C.B.); isaac_chiu@hms.harvard.edu (I.M.C.)
†These authors contributed equally to this work.
‡These authors contributed equally to this work.

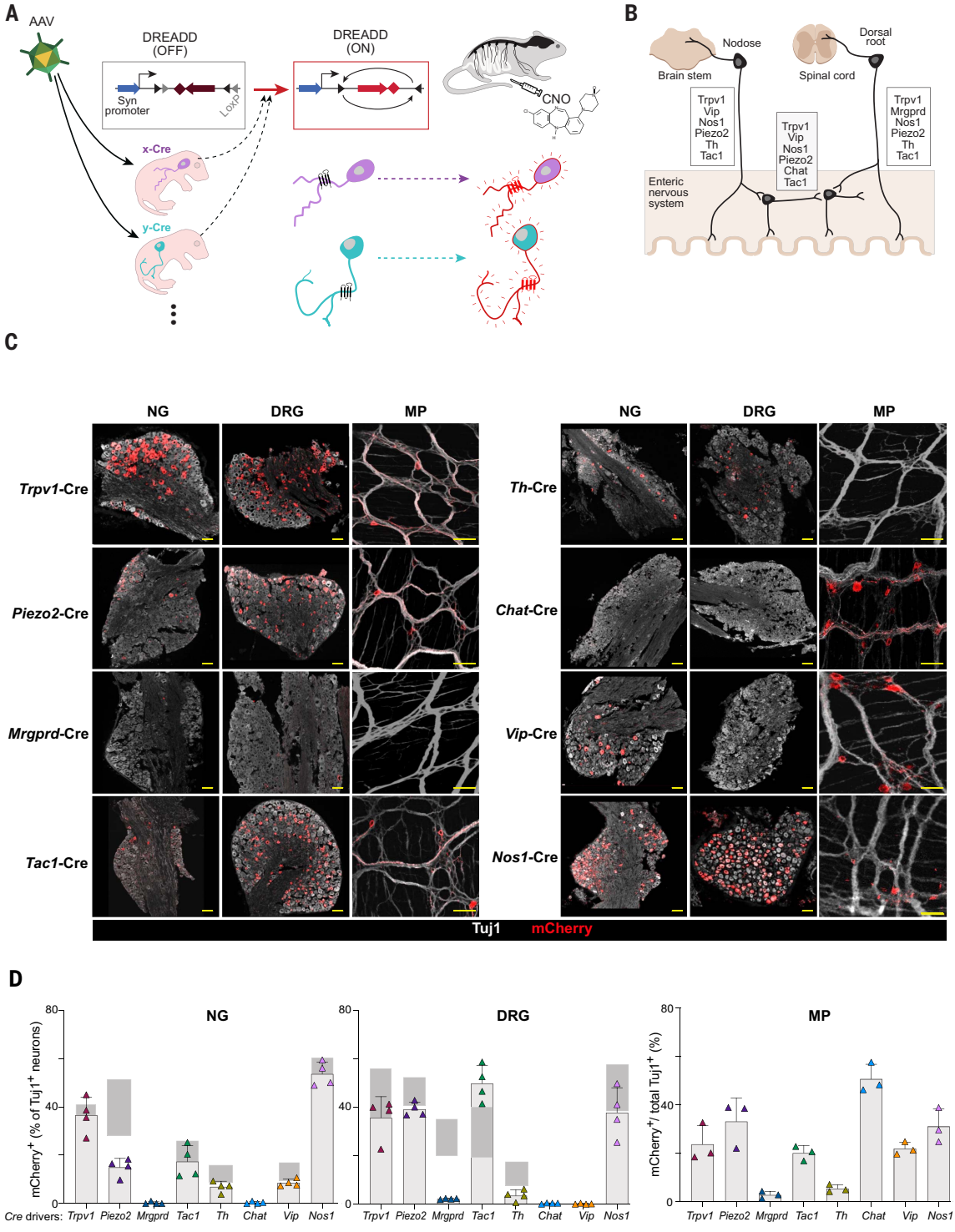

Fig. 1. Screening neuronal subtypes for immunomodulatory capabilities using viral-mediated DREADDs. (**A**) Schematic of experimental procedures describing the setup of DREADD-based chemogenetic screen for neuronal effects on the gut immune system. (**B**) Diagram showing neuronal subtypes in different anatomical locations (NG, DRG, and ENS) that innervate the gut and markers expressed in each location. (**C**) Representative confocal images of mCherry (red) and Tuj1 (β-III tubulin, gray) staining in the NG, DRG, and MP of the ENS after AAV.PhP.S-hSyn-DIO-mCherry-DREADD labeling of eight Cre lines. Scale bars are 100 μm. (**D**) Quantification of mCherry expression patterns across the eight Cre lines in the DRG, NG, and MP. For the DRG and NG, the proportion of mCherry$^+$ cells out of total Tuj1$^+$ cells were quantified (four or five fields per mouse, each point is the mean for an individual mouse, four mice per group, average ± SEM is shown). For the MP, the area labeled by mCherry out of the total Tuj1 area was quantified. Gray bars indicate the expected expression range for marker genes.

of the ENS (*Chat-cre*, *Nos1-cre*, *Vip-cre*, *Tac1-cre*), sensory neurons in the vagal jugular ganglia and NG (*Trpv1-cre*, *Vip-cre*, *Nos1-cre*, *Piezo2-cre*, *Tac1-cre*, *Th-cre*), and sensory neurons in the DRG (*Trpv1-cre*, *Tac1-cre*, *Mrgprd-cre*, *Piezo2-cre*, *Th-cre*, *Nos1-cre)* (Fig. 1B). The *Th-cre* and *Chat-cre* lines also target postganglionic sympathetic neurons and parasympathetic neurons, respectively.

To confirm expression of the DREADD in neurons of the injected mice, we stained sections of the NG, DRG, and the ENS myenteric plexus (MP) in the colon with antibodies against the pan-neuronal marker β-III tubulin (Tuj1) and mCherry (Fig. 1C). The NG and DRG showed labeling of mCherry$^+$ neuronal cell bodies, whereas the colon showed both ENS MP cell bodies and fibers that may represent either intrinsic or extrinsic innervation. Whereas the NG, DRG, and MP were clearly labeled for mCherry and Tuj1, submucosal plexus showed greater variability in staining and were not imaged. Quantification of mCherry expression, out of total neurons in each Cre line, showed expression in the DRG, NG, or MP that fit expected patterns for the transgenic markers (Fig. 1D), with frequencies of labeling close to,

but lower than, those expected from known marker or reporter expression. Labeling in *Mrgprd-creErT2* mice, which required tamoxifen injection for Cre induction, was present but less abundant than expected, possibly because of low or mistimed Cre expression. We did observe some Trpv1 and Piezo2 expression in intrinsic neurons (Fig. 1, C and D). Overall, this intersectional chemogenetic approach limited DREADD expression to defined neuron classes, and to sizeable proportions of these.

DREADD-based activation of specific neurons elicits distinct changes in gut immunocyte pools

After confirming the specificity and efficiency of this AAV.PhP.S^{hM3Dq} Cre-based activity, we investigated the changes within intestinal populations of immunocytes induced by chemogenetic activation of various neurons. Mice were infected neonatally with AAV.PhP.S^{hM3dq} and treated at adult age with CNO (hereafter abbreviated as "ADC" mice) every other day over a 2 week period. Lymphoid and myeloid cells from different intestinal locales (ileum, cecum, colon) were then analyzed by high-parameter flow cytometry to examine 31 immunophenotypes (fig. S2A). For robustness, each experiment included ADC mice and Cre-negative control littermates that were also injected with AAV.PhP.S^{hM3Dq} and treated with CNO (hereafter "CTRL" mice). In Trpv1-ADC mice, but not CTRL mice, CNO injection induced c-FOS expression in spinal cord dorsal horn neurons by 1.5 hours after injection, which remained at 7 hours but cleared by 24 hours (fig. S1B). These data indicate a kinetic of chemogenetic activation that lasts for several hours after injection, in keeping with usual observations with this compound (*35*, *36*).

Several neuroimmune relationships were detected for which activation of a neuronal subset led to distinct changes in immunophenotypes (Fig. 2, A to F; tabulated as proportional values in Fig. 2G; and as numbers per 1,000,000 CD45$^+$ cells, reflecting standardized immune cell numbers in gut lamina propria, in data S3). Some relationships were very exclusive. Nos1$^+$ nitrergic neuron activation down-regulated RORγ^+ CD4$^+$ conventional T [T helper 17 (T_H17)–like] cells in the ileum in Nos1-ADC mice compared with CTRL mice (Fig. 2A), whereas Chat$^+$ cholinergic neuron activation down-regulated ileal neutrophils (Fig. 2B). Mrgprd$^+$ neuron activation led to increased ileal populations of MHCII$^+$ mononuclear phagocytes (MNPs) (Fig. 2C). These three effects were specific to the ileum, with no corresponding counterpart in the cecum or colon (fig. S2, B to D).

Activation of Trpv1$^+$ sensory neurons affected several cell populations: ILC2s in the colon (Fig. 2D), RORγ^+ T_{reg} cells in both the colon and cecum (Fig. 2, E and F), and also, but more modestly, total colonic T_{reg} cells, colonic macrophages, and the CD44$^+$ fraction of colonic CD8$^+$ T cells (Fig. 2G and figs. S2, E to G, and S3). Some immunocyte populations were not affected by activation of any neuronal subtypes tested (B, γδ T, and natural killer cells; Fig. 2G and fig. S2, H to J). Activation of some neurons (Piezo2, Th, or VIP) did not seem to influence the homeostatic setting of gut immunocytes (Fig. 2G).

Neuronal types that had effects on immunocyte populations were found among the various origins of intestinal innervation (NG, DRG, or ENS; Fig. 1B). Thus, the screen uncovered a patchwork of discrete alterations induced by chemogenetic activation of distinct neuronal types, with Trpv1$^+$ nociceptor neurons having the most widespread effects.

DREADD-based neuronal activation induces modest changes in gut microbiota

Many situations have been described in which alterations in gut microbes influence the peripheral nervous system (*1*, *37*, *38*), and there are a few cases where perturbations of gut-innervating neurons reflect on the intestinal microbiota (*39*, *40*). We investigated whether the specific neuronal activation in ADC mice provoked dysbiosis, an imbalance in the gut microbiome that could be a confounder for the interpretation of the immunophenotypes observed, or rather elicited specific effects on a microbial family or genus.

Bacterial populations were profiled in colonic content from ADC and CTRL littermates by 16*S* ribosomal DNA (rDNA) amplification and sequencing (testing littermate pairs to eschew cage-of-origin issues). There was no indication of strong dysbiosis in any of the mice, given that α-diversity in ADC and CTRL littermates was generally comparable (fig. S4A). A few of the Trpv1-ADC mice showed lower microbial diversity, but these mice did not have particularly low colonic RORγ^+ T_{reg} cells or other immunologic changes. Principal components analysis also showed no marked deviation between ADC and CTRL littermates (fig. S4B). Closer examination at the phylum level showed a modest but statistically significant increase in the abundance of Bacteroidetes in Trpv1-ADC, with a corresponding decrease in Firmicutes (fig. S4C), which is of interest because of a previous report that disruption of intestinal Trpv1 innervation led to an increase in Bacteroidetes (*40*). This deviation in Bacteroidetes-Firmicute balance was confirmed in a replication cohort of Trpv1-ADC mice (fig. S4D) and occurred in both male and female mice (fig. S4E). Analysis of finer taxonomic ranks failed to reveal changes in Trpv1-ADC or other ADC mice beyond the level of experimental noise or that were reproducible in the replication cohort. The exception was a 25-fold increase in abundance of *Clostridiaceae* in Tac1-ADC mice (data S4).

The small shifts in relative abundances of Firmicutes versus Bacteroidetes were unlikely to explain changes in T_{reg} cell abundance, given that both phyla contain many T_{reg} cell inducers (*41*), and there was no correlation between RORγ^+ T_{reg} cells and Firmicutes or Bacteroidetes relative abundances in individual Trpv1-ADC mice (fig. S4, F and G). Thus, activation of the wide range of intestinal neuronal types in our panel did not induce large reorganization of the gut microbiota, beyond modest shifts in phylum representation.

Trpv1$^+$ neurons control the gut T_{reg} cell niche

We focused subsequent experiments on our findings that RORγ^+ T_{reg} cells decreased in frequency after activation of Trpv1$^+$ neurons, a decrease that was robust and reproducible (Fig. 2). Trpv1$^+$ neurons mediate nociception of noxious heat and capsaicin (*42*) and mainly reside in the DRG and NG. The frequency of RORγ^+ T_{reg} cells (*43*) is modulated by gut microbes and helps control tissue inflammation and oral tolerance and helps maintain peaceful coexistence at the host-symbiont interface (*43*, *44*). Most germane here, we showed previously that the control of RORγ^+ T_{reg} cells by gut microbes is associated with perturbations of the ENS, proposing a triangular interaction between gut microbes, RORγ^+ T_{reg} cells, and the intestinal nervous system (*45*, *46*). A vagal brain-gut arc has also been proposed to maintain gut T_{reg} cells (*47*).

RORγ^+ T_{reg} cells result in part from conversion of FoxP3-negative conventional T (T_{conv}) cells in the intestinal lymphoid tissues, but there is some debate whether this conversion takes place in the draining lymph nodes or in the lamina propria. Here, the effect of Trpv1$^+$ neuron activation was visible in the lamina propria, but not in the mesenteric lymph nodes (mLNs) (Fig. 3A), as was the reduction in total T_{reg} cells. This suggested that neuronal activation influenced immune cells in the intestinal wall and not in the draining lymph nodes. T_{reg} cell populations were unchanged in the lungs or mLNs (Fig. 3A). The spleen of Trpv1-ADC mice showed a reduction of RORγ^+ T_{reg} cells (Fig. 3A), a small population that is likely to result from trafficking from the gut to the systemic lymphoid organs (*48*–*50*). Thus, the consequences of neuroimmune interactions in the gut seem to be reflected more systemically.

Thetis or Janus cells, a recently described class of unconventional antigen presenting cells, control RORγ^+ T_{reg} cell frequencies (*51*, *52*). In the mLNs of Trpv1-ADC mice, we did not detect changes in Thetis or Janus cells (which were identified and distinguished using the marker combination, MHCII$^+$IL7R$^-$CXCR6$^-$) after activation (fig. S5A), indicating that these cells are not an intermediate for Trpv1-ADC effects.

To elucidate the mechanism that connects Trpv1$^+$ neuron activation and RORγ^+ T_{reg} cells, we determined the kinetics of the response:

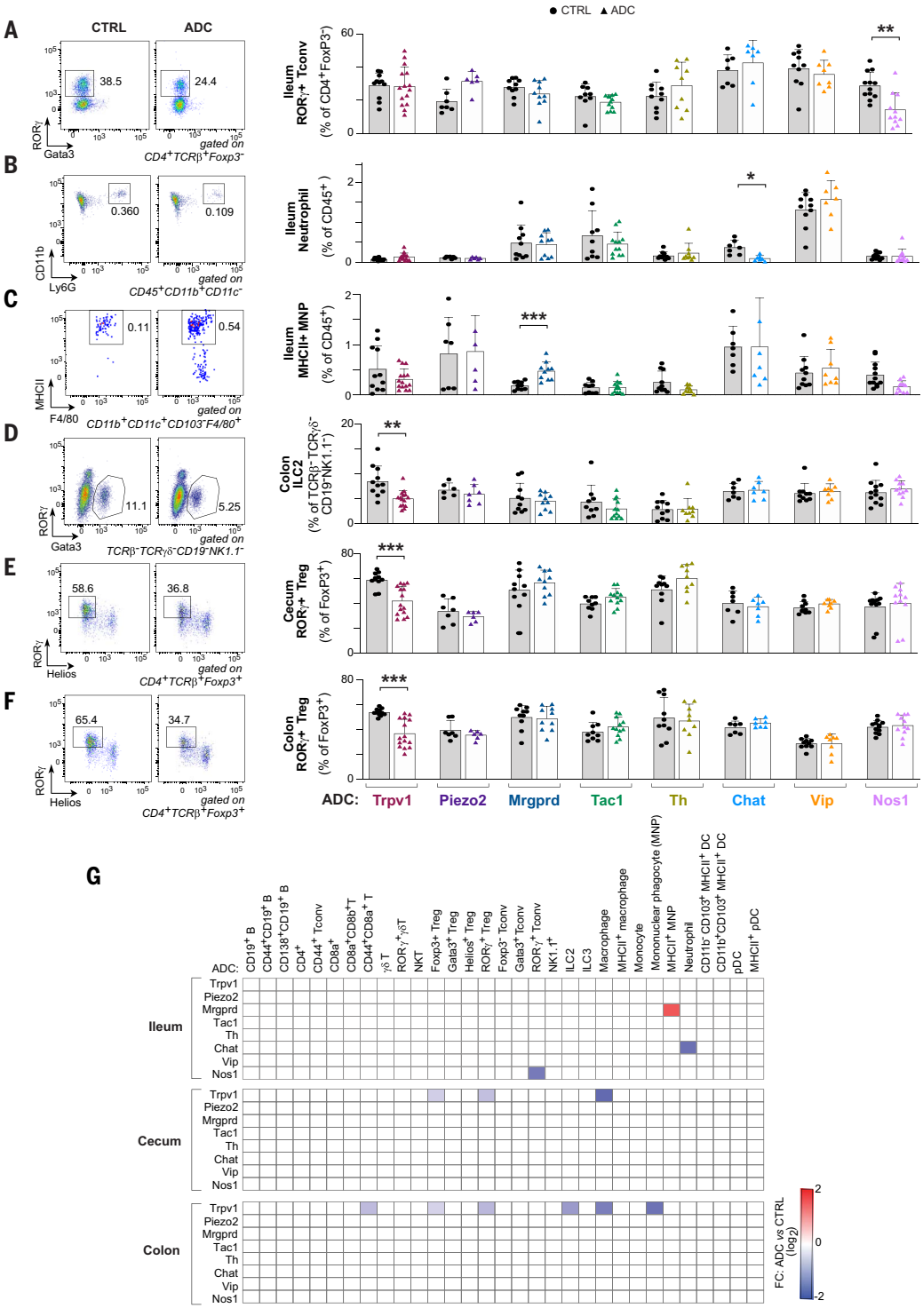

Fig. 2. Distinct gut immune changes after DREADD-mediated neuronal activation. (**A** to **F**) Quantification of proportions of ileum RORγ$^+$ T_{conv} cells (A), ileum neutrophils (B), ileum MHCII$^+$ MNPs (C), colon ILC2s (D), colon RORγ$^+$ T_{reg} cells (E), and cecum RORγ$^+$ T_{reg} cells (F) with representative flow cytometric plots (gated as indicated) after chemogenetic activation of different neuronal subsets in distinct ADC mice (color coded) and CTRL mice (gray bars). The full gating strategy can be found in fig. S2A. (**G**) Heatmap of average fold changes (FC), ADC versus CTRL, for significantly changed immune cell populations in the ileum, cecum, and colon from each Cre line compared with CTRL littermates after CNO treatment ($P < 0.05$). White squares indicate $P > 0.05$. Each symbol in (A) to (F) represents an individual mouse; bars represent mean, and error bars are standard deviation. *$P < 0.05$, **$P < 0.01$, and ***$P < 0.001$ (Student's t test with Holm-Sidak correction for multiple comparison). Data are representative of ≥2 independent experiments. $n = 7$ to 12 mice per group (both male and female).

Was the decrease in RORγ$^+$ T_{reg} cells fast, perhaps from cell death, or did it represent a slower change in homeostatic set points? The frequencies of RORγ$^+$ T_{reg} cells were not affected 1 day after CNO treatment, and the decrease in RORγ$^+$ T_{reg} cells was not fully evident until 2 weeks of activation (Fig. 3B), suggesting that the changes resulted from slow adaptation. However, the decreased RORγ$^+$ T_{reg} cell frequencies did not represent a stably altered set point: Three weeks after cessation of treatment, the frequencies had reverted back to normal (Fig. 3C).

A slow reduction in the frequency of RORγ$^+$ T_{reg} cells in the colon and cecum could be due to induced extravasation from the gut, cell death, and/or decreased proliferation from a reduced trophic support. To assess the turnover of intestinal T_{reg} cells, we bred *Trpv1*-Cre mice with transgenic mice encoding the photoconvertible Kaede fluorescent protein (*53*). In Kaede mice, colon cells can be temporarily switched from green to red by colonoscopic illumination with violet light, and both their residence in the colon and emigration into systemic organs can be tracked over time (*48*, *49*, *54*). In Trpv1-ADC mice, CNO treatment did not reduce

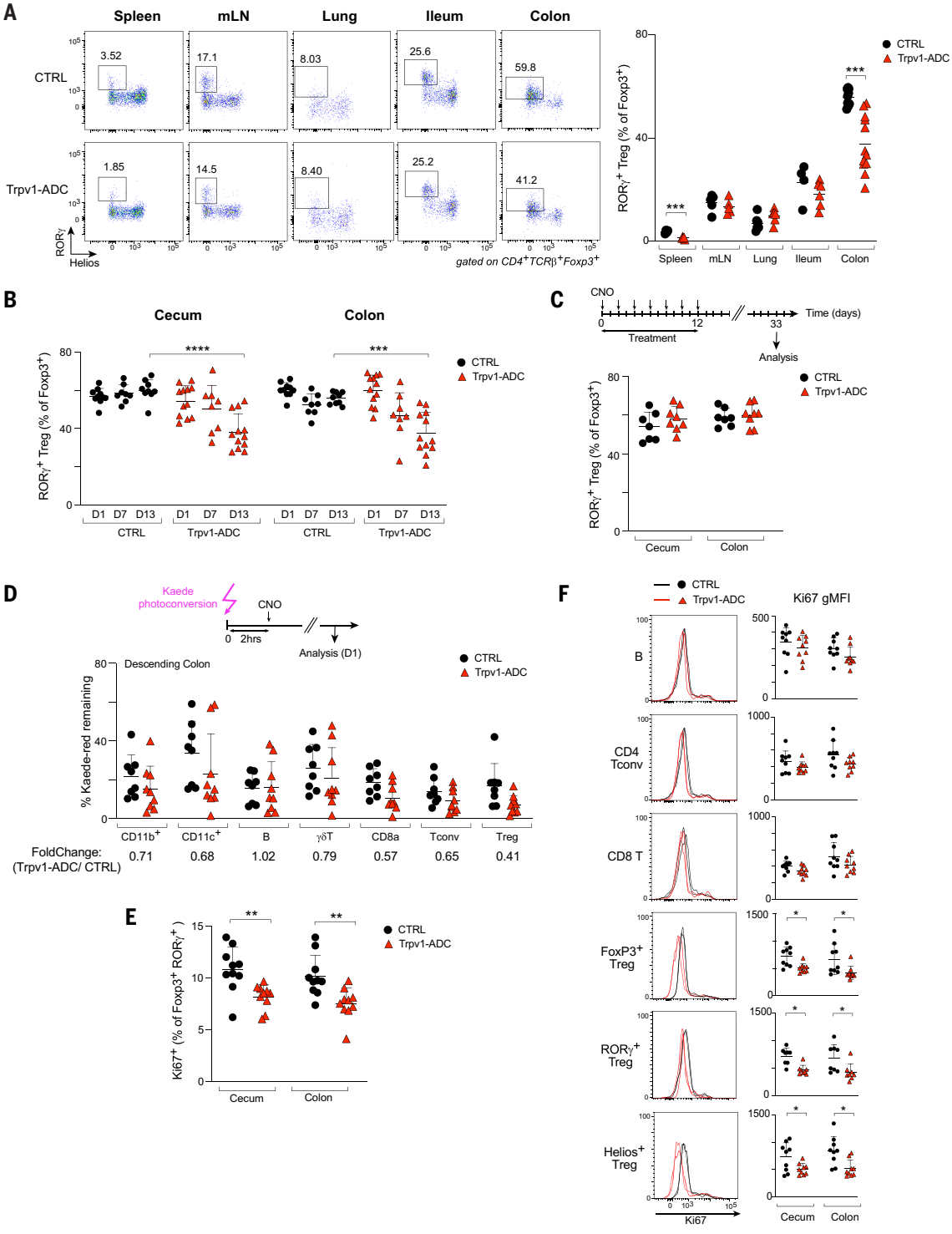

Fig. 3. Trpv1$^+$ neurons control the gut T_{reg} cell niche. (**A**) Representative flow cytometric plots and quantification of proportions of RORγ^+ T_{reg} cells in the spleen, mLN, lung, ileum, and colon tissues from Trpv1-ADC and CTRL littermates. The full gating strategy can be found in fig. S2A. (**B**) Quantification of proportions of RORγ^+ T_{reg} cells in the cecum and colon of Trpv1-ADC and CTRL mice from indicated time points after CNO treatment (day 1, day 7: CNO injected daily; day 13: CNO injected every other day). (**C**) Quantification of proportions of RORγ^+ T_{reg} cells in the cecum and colon of Trpv1-ADC and CTRL mice from the indicated time points. (**D**) Quantification of proportions of Kaede red–positive immune cells in the descending colon from Trpv1-ADC-Kaede and CTRL littermates. (**E**) Quantification of proportions of Ki67$^+$ cells (of RORγ^+ T_{reg} cells) in the cecum and colon from Trpv1-ADC and CTRL mice. (**F**) Representative flow cytometric plots and quantification of geometric mean fluorescence intensity (gMFI) of Ki67 (of B, CD4 T_{conv}, CD8 T, FoxP3$^+$, RORγ^+, and Helios$^+$ T_{reg} cells) in the cecum and colon from Trpv1-ADC and CTRL mice. Each symbol in (A) to (F) represents an individual mouse; bars represent mean, and error bars are standard deviation. *P < 0.05, **P < 0.01, ***P < 0.001, and ****P < 0.0001 (unpaired Student's t test with Holm-Sidak correction for multiple comparison). Data are representative of ≥3 independent experiments. n = 5 to 12 mice per group (both male and female).

photoconversion efficacy but slightly lowered the proportion of photoconverted cells that remained in the descending colon after 24 hours (Fig. 3D), indicating that Trpv1$^+$ neuron activation increased immunocyte turnover slightly. This was observed for most cell types, not specifically RORγ^+ T_{reg} cells (Fig. 3D), which suggests that increased turnover was not the driving force in the reduction in the frequency of RORγ^+ T_{reg} cells. Annexin-V staining showed that the proportion of dying cells did not increase after neuronal activation (fig. S5B). We assessed T_{reg} cell proliferation by staining for the nuclear factor Ki67. Ki67 has a complex relationship with the cell cycle because it is actively synthesized during S, G_2, and M phases and then is progressively degraded during G_1 and G_0, thus serving as a marker of the time since the last division (*55*). T_{reg} cells in Trpv1-ADC mice showed a slightly decreased proportion of Ki67^{hi} RORγ^+ T_{reg}

cells compared with their CTRL littermates (Fig. 3E). A shift was noted in the noncycling peak, which lost Ki67 intensity in T_{reg} cells but not in other gut lymphocytes (Fig. 3F). No such changes were observed in other tissues (fig. S5, C and D), save for splenic T_{reg} and B cells. Overall, these data suggest that nociceptor activation decreases the RORγ^+ T_{reg} cell pool by curtailing the proportion of T_{reg} cells that are poised to enter the cell cycle.

Trpv1$^+$ *neuron activation alters gut susceptibility to* Citrobacter *and DSS challenge*

Colonic T_{reg} cells contribute to maintaining gut barrier integrity and to regulating immunopathology (*43*). Thus, we asked whether Trpv1$^+$ neuron activation had functional consequences. At the end of the 2-week activation period by CNO treatment, we fed mice dextran sodium sulfate (DSS) to induce colitis. Trpv1-ADC mice displayed more severe weight loss than did their CTRL littermates, not during the initiation phase but during the recovery phase (fig. S6A), with higher inflammation being detected by histological analysis (fig. S6B). We also infected mice with *Citrobacter rodentium*, an attaching and effacing bacterial pathogen that induces colon inflammation and pathology in mice (*56*). Trpv1-ADC mice lost more body weight than CTRL mice (fig. S6C). In addition, even though their gut colonization with *C. rodentium* was comparable to that of CTRL mice (fig. S6D), many of the Trpv1-ADC mice showed systemic dissemination of the bacterium to the spleen and liver (fig. S6E).

To understand whether nociceptor activation affected ongoing gut inflammation, we induced low-grade inflammation with low-dose (1.5%) DSS for 3 weeks, a regimen in which the inflammation tends to resolve spontaneously. Upon CNO treatment during this course, Trpv1-ADC mice diverged from their CTRL littermates (fig. S6, F to H). Thus, nociceptor activation resulted in decreased levels of RORγ^+ T_{reg} cells and modulated gut inflammatory responses in both acute and longer-term models of inflammation.

Trpv1$^+$ *neuron activation elicits changes in immunocyte transcriptomes*

Having observed the effects of sensory neuron activation on colonic T_{reg} cells, and to start elucidating the functional connection, we investigated the intestinal ecosystem in general. Overall, histological analysis revealed no notable change in the general architecture of the colon, with no inflammatory infiltrate or tissue destruction (fig. S7A). The architecture of the MP did not show major distortion in Trpv1-ADC mice, as evidenced by Tuj1 staining (fig. S7B). These results indicated that Trpv1$^+$ neuron activation did not grossly affect the immunologic or neurologic architecture in the colon.

To investigate possible intermediate events between Trpv1$^+$ neuron activation and changes in RORγ^+ T_{reg} cells, we performed scRNA-seq on total CD45$^+$ immunocytes from the cecum of Trpv1-ADC and CTRL mice. Dimensionality reduction and projection [uniform manifold approximation and projection (UMAP)] revealed all the common immunologic lineages expected in the cecum (Fig. 4A), which were identifiable by lineage-defining transcripts (fig. S8A), with equivalent distributions in all four mice profiled (fig. S8B). Comparing the relative cell density in these populations from Trpv1-ADC and CTRL mice revealed shifts in some immunocytes, most markedly in lymphoid cells and less so in myeloid cells (Fig. 4B). To identify immunocyte transcripts perturbed by Trpv1$^+$ neuron activation, while avoiding those appearing differential because of altered cell-type representation, we performed differential gene expression analysis separately on individual cell populations, tallying the resulting most affected 187 transcripts on the heatmap of Fig. 4C (fig. S8C and data S5). Trpv1$^+$ neuron activation had a mild but broad impact on gene expression across cell types. Gene cluster c1, induced in almost all cell types, was almost exclusively composed of heat-shock proteins and other stress response genes (*Hspa1a/b*, *Hsp8*, *Hsp90*, *Dnajb1*), suggesting that immunocyte stress resulted from Trpv1$^+$ neuronal activation. Only a minority of transcripts from a prototypical signature of cell damage (*57*) were up-regulated (fig. S8D), indicating that the stress response to neuron activation had specificity and was not merely uncontrolled cell damage. Two other clusters (c4, c5) were most prominently altered in intraepithelial lymphocyte (IEL)–like T cells, but were also altered in other cell types, and formed a network enriched in cytokine receptors (*Tnfrsf1*, *Il21r*, *Ifngr1*) and cell signaling (*Lyn*, *Itk*, *Map3k1*) and transcriptional regulators (e.g., *Nfkb1*, *Stat3*, and *Stat4*) (fig. S8E), suggesting that neuronal activation might modulate intercellular communication between immunocytes.

We recomputed a UMAP focused on T_{reg} cells alone, which identified RORγ^+, Helios$^+$, and double-negative T_{reg} cells (Fig. 4D) substantiated by the expression of signature genes (*58*) (fig. S8F). Many of the changes seen in bulk T_{reg} cells (Fig. 4C) were observed in both RORγ^+ and Helios T_{reg} cells (fig. S8G), suggesting that they may not themselves discriminate between T_{reg} cell subsets. Comparing relative cell frequencies (Fig. 4E) revealed a focused reduction that affected only a segment of the RORγ^+ T_{reg} cell group (group "A" in Fig. 4E) but not the other ("B"). We then asked what genes distinguish, in CTRL mice devoid of chemogenetic neuronal activation, those RORγ^+ T_{reg} cells destined to be reduced electively by Trpv1$^+$ neuron signaling (group A), relative to their more resistant group B counterparts (Fig. 4F). Interestingly, several of the differential transcripts revealed by this A versus B comparison within CTRL T_{reg} cells belonged to those altered by Trpv1$^+$ neuron activation (*Hsp* family; data S6). That this signature of sensory neuron activation in T_{reg} cells preexists in normal RORγ^+ T_{reg} cells suggests that the neuron–T_{reg} cell cross-talk is already in play in normal unperturbed mice, in response to physiological triggers.

Trpv1$^+$ *spinal afferent neurons are responsible for altering the* T_{reg} *cell niche*

After characterizing the immunocyte changes induced by activation of Trpv1$^+$ neurons, we aimed to determine the neuronal mechanisms that led to T_{reg} cell modulation. Trpv1 is expressed in two main anatomical locations, DRG neurons that centrally project to the spinal cord and NG neurons that project via the vagus nerve to the brainstem (*8*, *9*) (fig. S1B). Given that our chemogenetic strategy would label and activate all these neurons, we investigated the relative contribution of the two Trpv1$^+$ neuron locations (*59*, *60*).

To target Trpv1$^+$ neurons in the NG, we performed bilateral intranodose injections of AAV9^{hM3Dq} virus in *Trpv1-cre* mice or CTRL littermates (Fig. 5A). Intranodose injection yielded robust DREADD-mCherry expression in NG neurons, with no labeling of DRG neurons (Fig. 5B). In these mice, chemogenetic activation by CNO treatment did not elicit changes in colonic RORγ^+ T_{reg} cells or any other immunocyte populations relative to CTRL littermates (Fig. 5C and fig. S9A). To target DRG neurons, we injected AAV9^{hM3Dq} virus intrathecally into the lumbar spinal column of *Trpv1-cre* mice or CTRL littermates (Fig. 5D), resulting in specific expression of DREADD-mCherry in DRG, but not vagal, neurons (Fig. 5E). Chemogenetic activation of DRG Trpv1$^+$ neurons by 2 weeks of CNO treatment decreased cecal and colonic RORγ^+ T_{reg} cells and macrophages in intrathecally injected mice, suggesting that DRG Trpv1$^+$ neurons modulated multiple immunocyte populations, as we observed for whole-body Trpv1$^+$ neuron activation (Fig. 5F and fig. S9B). Together, these data indicate that activation of sensory Trpv1$^+$ neurons in the DRG, but not of vagal neurons, was sufficient to induce T_{reg} cell population changes in the GI tract.

We next determined whether DRG neurons were necessary for Trpv1$^+$ neuronal regulation of T_{reg} cells. We generated Trpv1-ADC mice, in which we performed targeted ablation of DRG Trpv1$^+$ neurons by intrathecal injection of resiniferatoxin (RTX), a high affinity Trpv1 agonist that causes the loss of Trpv1$^+$ neurons (*61*) (Fig. 5G). Mice treated with intrathecal injection of RTX had greatly diminished DREADD-mCherry expression in the DRG while sparing those neurons in the NG (Fig. 5H). After chemogenetic activation by CNO treatment, Trpv1-ADC

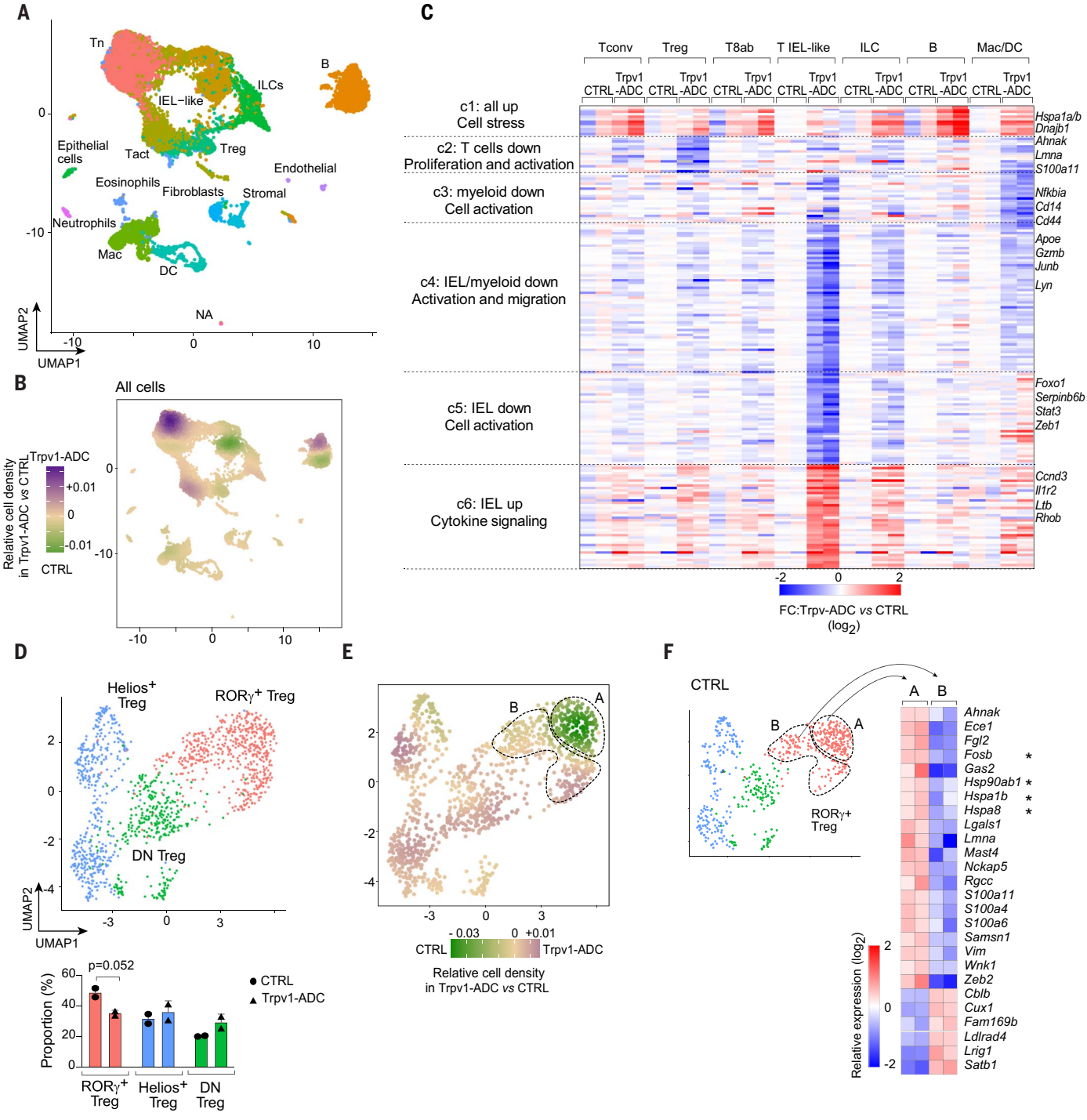

Fig. 4. scRNA-seq reveals cell stress and cell activation upon nociceptor neuron activation. (**A**) UMAP plot of scRNA-seq cecum immunocytes from Trpv1-ADC and CTRL mice (two mice each, hashtagged into one experiment, 18,130 cells total). DC, dendritic cell; Mac, macrophage; NA, unidentified; Tact, activated T cell; Tn, naïve T cell. (**B**) Data from (A) as a representation of differential cell density in Trpv1-ADC versus CTRL mice (green and purple indicate cells under- and overrepresented in Trv1-ADC, respectively). (**C**) Heatmap of average expression fold changes (Trpv1-ADC versus CTRL mice, log2) of differentially expressed genes extracted from seven cell clusters as indicated. Mac/DC, macrophages and dendritic cells; T8ab, $CD8a^{+}CD8b^{+}$ T cells. (**D**) Data from (A) analyzed by UMAP recomputed to consider only T_{reg} cells, color coded by Louvain clusters (Seurat) and identified from signature expression of colon T_{reg} cell subsets, with proportions compared in the histogram below ["Proportion" indicates the percentage of each T_{reg} cell subpopulation of the total T_{reg} cells. Cell count (generated by Seurat): Total:$ROR\gamma^{+}$ T_{reg}:$Helios^{+}$ T_{reg}:DN T_{reg}, CTRL.1 = 287:131:99:57; CTRL.2 = 329:169:93:67; Trpv1-ADC.1 = 310:113:95:102; Trpv1-ADC.2 = 368:124:151:93]. (**E**) Data from (D) shown as differential density between CTRL and Trpv1-ADC mice, color coded as in (B). Regions A and B denote groups of $ROR\gamma^{+}$ T_{reg} cells differently affected by Trpv1-ADC activation. (**F**) Genes differentially expressed between $ROR\gamma^{+}$ T_{reg} cells of groups A or B [as defined in (E)] from the two CTRL mice only (shown as log2 relative expression). Asterisks indicate genes found in c1 in (C). Each symbol in (D) represents an individual mouse; bars represent mean, and error bars are standard deviation (unpaired Student's *t* test). *n* = 2 mice per group.

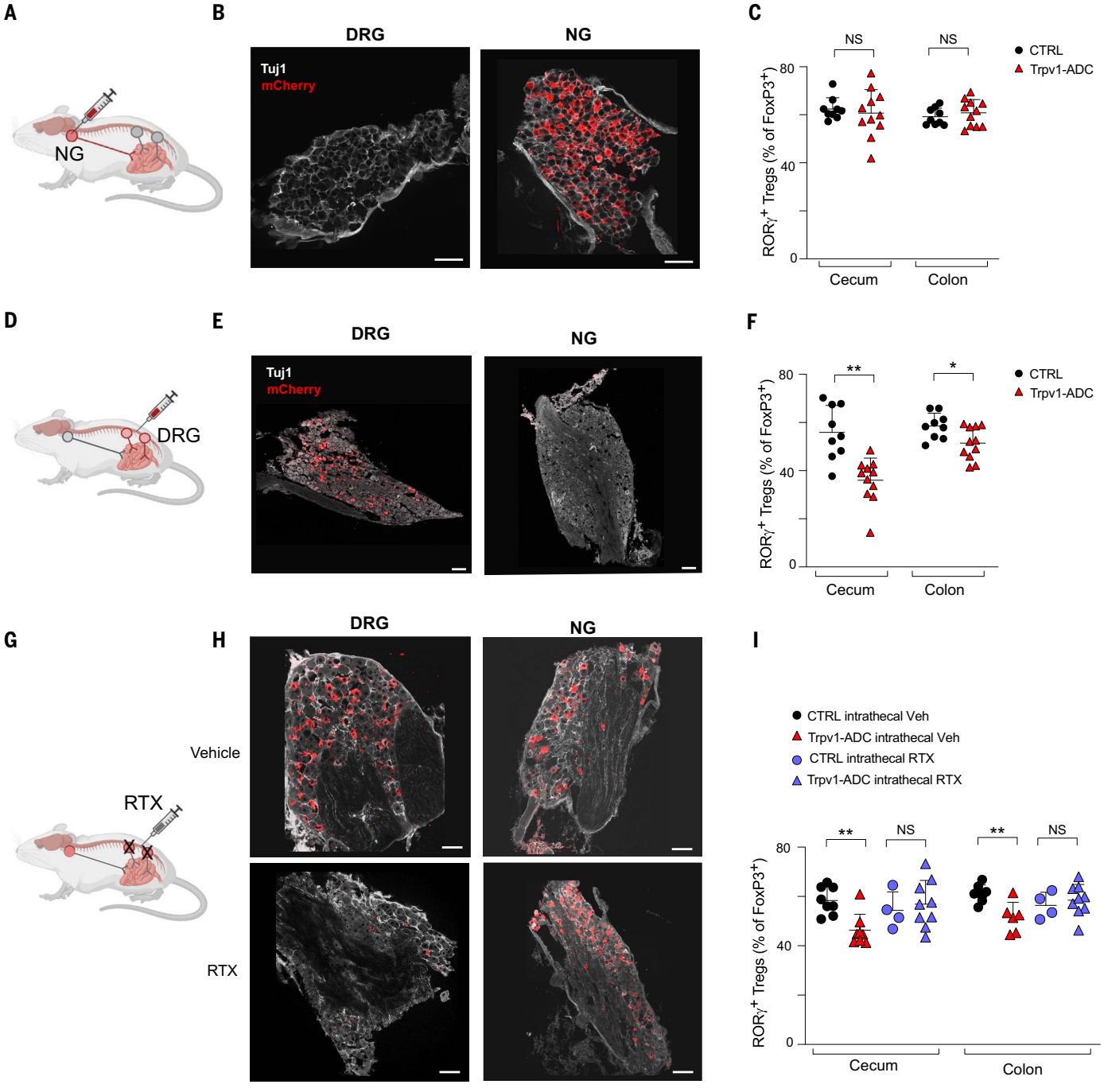

Fig. 5. Trpv1$^+$ DRG neurons, but not NG neurons, regulate the gut T_{reg} cell niche. (**A**) Schematic of intranodose ganglionic injection into *Trpv1*-Cre and CTRL mice for targeting of AAV9^{hM3Dq} virus to NG and jugular ganglia. (**B**) Representative confocal images of mCherry (red) and Tuj1 (gray) staining in the DRG and NG after intranodose injection. (**C**) Quantification of RORγ$^+$ T_{reg} cells in the cecum and colon from intranodose ganglionic–injected *Trpv1*-Cre and CTRL mice. (**D**) Schematic of intrathecal injection into *Trpv1*-Cre and CTRL mice for targeting of AAV9^{hM3Dq} virus to DRG neurons. (**E**) Representative confocal images of mCherry (red) and Tuj1 (gray) staining in the DRG and NG of intrathecally injected mice. (**F**) Quantification of RORγ$^+$ T_{reg} cells in the cecum and colon from intrathecally injected *Trpv1*-Cre and CTRL mice. (**G**) Schematic of RTX intrathecal injection for ablation of Trpv1$^+$ DRG neurons. (**H**) Representative confocal images of mCherry (red) and Tuj1 (gray) staining in the DRG and NG of Trpv1-ADC mice injected intrathecally with vehicle or RTX. (**I**) Quantification of RORγ$^+$ T_{reg} cells in the cecum and colon from Trpv1-ADC and CTRL mice with intrathecal injection of vehicle or RTX. Each symbol in (C), (F), and (I) represents an individual mouse; bars represent mean, and error bars are standard deviation. *P < 0.05, **P < 0.01, and NS is no significance (unpaired Student's t test with Holm-Sidak correction for multiple comparison). Scale bars are 100 μm in (B), (E), and (H). Data are representative of ≥2 independent experiments. n = 4 to 11 mice per group (both male and female).

mice treated with RTX did not down-regulate cecal and colonic RORγ$^+$ T_{reg} cells (Fig. 5I).

A previous study had reported that vagotomy and capsaicin injections into the vagus nerve altered colonic T_{reg} cell populations and proposed a brain-liver-gut sensory-autonomic circuit (*47*). However, our data indicate that spinal DRG Trpv1$^+$ neurons, but not vagal neurons, played a critical role in regulating RORγ$^+$ T_{reg} cells in the context of repeated nociceptor activation.

Trpv1$^+$ neurons regulate the gut T_{reg} cell niche through a CGRP-RAMP1 axis

After determining the Trpv1$^+$ neurons responsible for decreasing RORγ$^+$ T_{reg} cell frequencies, we wanted to elucidate the mechanism through which these neurons signal to the T_{reg} cells. In principle, this regulation could be through direct neuroimmune communication and/or indirectly via an intermediate cell type. Trpv1$^+$ neurons in the DRG are peptidergic (*62*), expressing neuropeptides including calcitonin gene–related peptide (CGRP) and substance P (SP) (fig. S10A). Given the role of these neuropeptides in regulating both vascular and immune responses in neurogenic inflammation (*63*), we hypothesized that Trpv1$^+$ neurons might release neuropeptides upon activation that could signal to and impair RORγ$^+$ T_{reg} cell turnover. SP is encoded by *Tac1*, which can also be spliced to encode neurokinins A and B (*64*). We intercrossed *Tac1*$^{-/-}$ with *Trpv1*-cre mice to generate Tac1-deficient Trpv1-ADC mice. In these animals, the reduction in total RORγ$^+$ T_{reg} cells in the colon after CNO treatment was similar to that of Trpv1-ADC mice (Fig. 6A), suggesting that SP and neurokinins were not required. Macrophage and ILC2 populations were also reduced in Trpv1-ADC mice (fig. S10B), indicating that SP was not essential for effects of neuronal activation in this model.

CGRP is expressed by two genes, *Calca* (encodes CGRPα) and *Calcb* (CGRPβ), whose products both bind to the same receptor complex and have similar functional activity (*65*). *Calca* is expressed at higher levels in the DRG than in enteric neurons, whereas *Calcb* is expressed in both the DRG and enteric neurons (*7*, *65*). Given our finding that DRG nociceptors regulated T_{reg} cells (Fig. 5), we crossed *Trpv1*-Cre mice with *Calca*$^{-/-}$ mice to deplete CGRPα. *Calca*$^{-/-}$ Trpv1-ADC mice did not show the usual decrease in colonic and cecal RORγ$^+$ T_{reg} cells compared with CTRL littermates treated with CNO (Fig. 6B), indicating an important role for CGRPα in nociceptor–T_{reg} cell cross-talk. However, the macrophage compartment was still down-regulated (fig. S10C), indicating a specific involvement of CGRPα in neuronal regulation of T_{reg} cells.

CGRP has been reported as a mediator in neuroimmune interactions (*66*, *67*) that involve several immunocytes of the innate immune system such as ILC2s (*68*–*70*), neutrophils (*71*, *72*) or dendritic cells (*73*). Thus, the effect of Trpv1$^+$ neuron activation on T_{reg} cells might be indirect, in line with observations in the injured muscle, where CGRP tunes interleukin-33 (IL-33) production by mesenchymal stromal cells, which then results in the accumulation of muscle T_{reg} cells (*74*). However, computational analysis of whole mounts of colon tissue showed a less-than-chance proximity between FoxP3$^+$ T_{reg} cells and CGRP-positive fibers of sensory neurons in the lamina propria. This might be consistent with the cells being able to interact directly (Fig. 6, C and D, and fig. S10D).

To test this hypothesis, we asked whether the CGRP receptor on T_{reg} cells was required for the Trpv1-ADC effect. CGRP acts on target cells by binding to a high-affinity receptor complex formed by CALCRL and modifying co-receptor RAMP1 (*65*) (Fig. 6E). In the scRNA-seq data, RAMP1 was preferentially expressed in RORγ$^+$ T_{reg} cells, relative to Helios$^+$ T_{reg} cells, providing a possible explanation for a preferential effect of Trpv1-ADC on RORγ$^+$ T_{reg} cells (Fig. 6F). To assess whether RAMP1 was required for Trpv1$^+$ neuronal signaling to T_{reg} cells, we treated mice with the RAMP1 antagonist BIBN4096 (*75*) or vehicle 1 hour before every CNO injection in Trpv1-ADC mice or CTRL littermates. This pretreatment reverted the action of neuronal activation, showing that RAMP1 blockade rescued the decrease in RORγ$^+$ T_{reg} cells that resulted from Trpv1$^+$ neuron activation (Fig. 6G). In addition, we generated RAMP1-deficient T_{reg} cells by crossing the *Ramp1*^{flox} conditional allele with *Foxp3-Cre* mice (in addition to *Trpv1-cre*) to ablate *Ramp1* in T_{reg} cells (because of the two Cre transgenes in these mice, *Ramp1* is also deleted in Trpv1$^+$ neurons, which should be irrelevant). These *Foxp3-creRamp1*$^{fl/fl}$ Trpv1-ADC mice did not show decreased colonic RORγ$^+$ T_{reg} cells after CNO treatment (Fig. 6H). Macrophage and ILC2 populations were still down-regulated (fig. S10E). Conversely, T_{reg} proportions in the cecum and colon were not affected in *Foxp3-creRamp1*$^{fl/fl}$ mice at baseline (fig. S10F), indicating that CGRP is not a dominant controller of T_{reg} cell homeostatic set points, which are known to reflect many different inputs (*43*). Together, these data suggest that CGRPα released from Trpv1$^+$ neurons upon chemogenetic activation bound to the RAMP1-CALCRL receptor complex on RORγ$^+$ T_{reg} cells and negatively regulated them, although CGRP did not affect long-term settings of the T_{reg} cell pools.

Discussion

Several recent studies have described the relationship between particular neuronal subsets and immunocytes in the gut (*10*–*12*, *14*, *16*–*18*, *70*, *76*–*78*). Our work extends understanding of this relationship by providing a more extensive and integrated view of neuroimmune interactions of relevance to the gut, which we accomplished by leveraging a panel of neuron subtype–specific DREADDs. We must acknowledge that there is a degree of artificiality in the approach because it involves coordinated GPCR-induced activation in many body locations. However, we chose our experimental design (repeated activation over a 2-week period instead of a single high-intensity burst) because it might reveal effects that occur over time and mimic conditions encountered in diseases in which peripheral neurons are chronically activated, such as in chronic pain, autonomic imbalance, or GI dysmotility (*79*–*81*). The adaptation and timing of observed changes in T_{reg} cell numbers after neuronal activation was similar to that resulting from microbe colonization, likely resulting from a resetting of homeostatic balance (e.g., by reducing proliferation rate), rather than rapid cell death.

We uncovered several neuron-immunocyte interactions that pointed to a broader involvement of neuronal types than had been hitherto recognized and will make for interesting future explorations. Nitrergic (Nos1$^+$) enteric neurons produce nitric oxide and mainly play an inhibitory role in peristalsis (*82*); their activation reduced the proportion of T_H17-like RORγ$^+$ T_{conv} cells in the ileum, possibly indicating a coordinated regulation of motor activity and type 3 and type 17 immune responses. Conversely, cholinergic (Chat$^+$) excitatory motor neuron activation decreased neutrophils in the ileum. It remains to be determined whether this finding relates to the cholinergic anti-inflammatory reflex, which was defined as acting through Chat$^+$ vagal neurons that operate through macrophages and T cells in the spleen (*83*). Because these immunocytes are functionally related in host defense (e.g., T_H17 cells and neutrophils) and these neuronal subsets coordinate motor function and peristalsis, one might speculate that motility and effector T cell responses might be coordinated. A minor activation of Mrgprd$^+$ sensory neurons boosted the proportion of MHCII^{hi} MNPs in the ileum. Mrgprd$^+$ neurons suppress mast cell activation through glutamate in the skin (*84*), but the role of Mrgprd$^+$ neurons in the gut is less well understood.

Amid this diversity, Trpv1$^+$ nociceptors were clearly those whose activation elicited the broadest and most robust changes, altering not only the gut RORγ$^+$ T_{reg} cell niche but also ILC2s, macrophages, and activated CD8$^+$ T cells (Fig. 2G). Transcriptome profiling revealed changes in an even broader set of immunocytes resulting from Trpv1$^+$ neuron activation. The most general effect was the increased expression of heat-shock and other stress response genes in most cell types, suggesting that signals from activated nociceptor neurons are interpreted as stress signals by immunocytes (Fig. 4C). Importantly, this induction

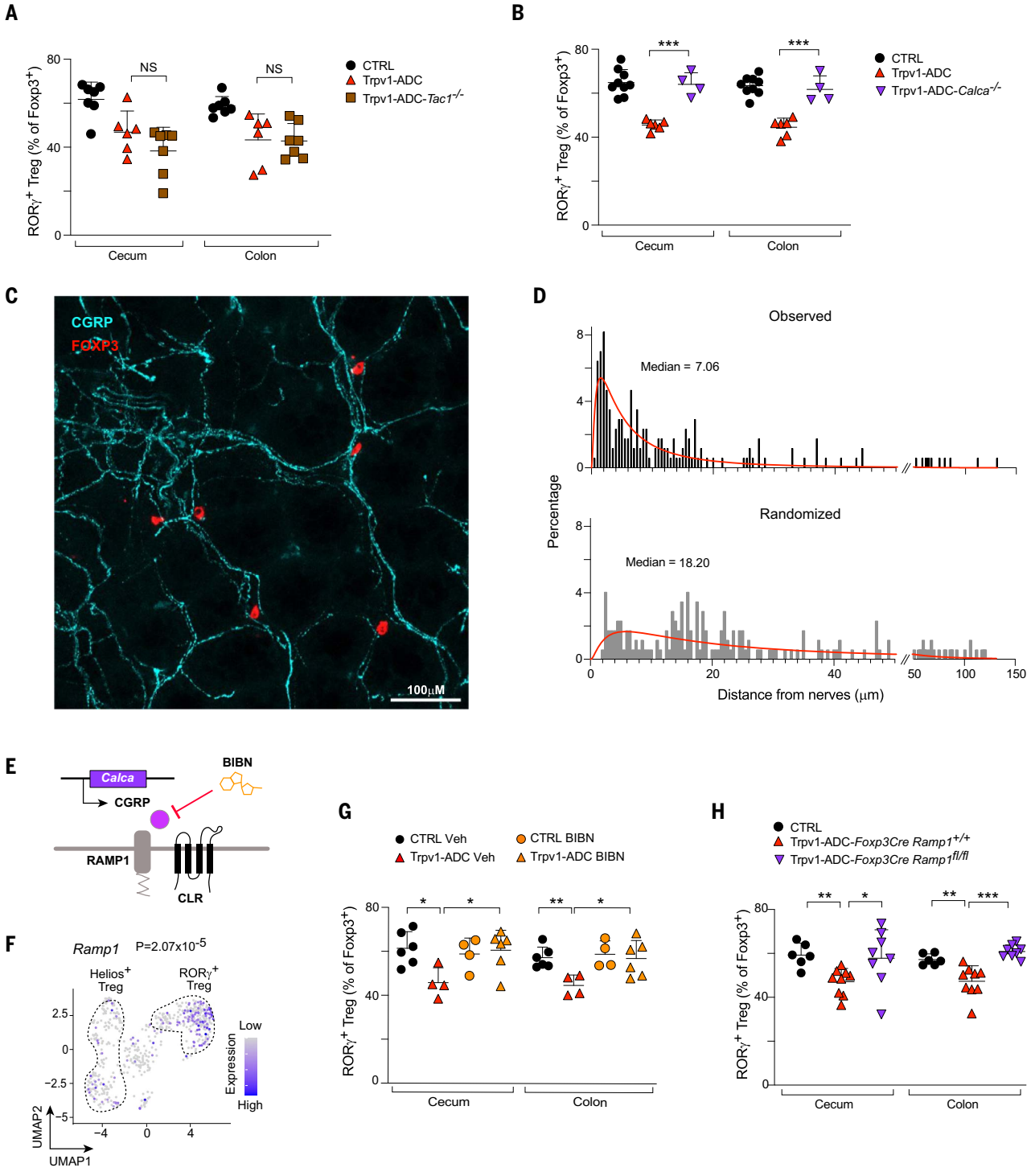

Fig. 6. Trpv1$^+$ neurons regulate the gut T_{reg} cell niche via CGRP. (**A**) Flow cytometric quantification of RORγ$^+$ T_{reg} cells in the cecum and colon from CTRL, Trpv1-ADC, and Trpv1-ADC-*Tac1*$^{-/-}$ mice (data generated and gated as in Fig. 2F). (**B**) Quantification of RORγ$^+$ T_{reg} cells in the cecum and colon from CTRL, Trpv1-ADC, and Trpv1-ADC-*Calca*$^{-/-}$ mice. (**C**) Representative confocal image of FoxP3$^+$ T_{reg} cells (red) in proximity to CGRP fibers (cyan) from whole-mount colon tissue. Scale bar is 100 μm. (**D**) Quantification of the distance of FoxP3$^+$ T_{reg} cells to CGRP$^+$ fibers (top) and randomized cells to CGRP$^+$ nerves (bottom) in the colon. Two sections from five mice were analyzed. The red lines represent the fitted linear regression of distance distribution. (**E**) Schematic of CGRP signaling through its co-receptor complex formed by RAMP1 and CLR. (**F**) UMAP of data from Fig. 4D (cells from the two CTRL mice only) showing *Ramp1* expression in T_{reg} cells (*P* value was generated by Seurat, a R toolkit for single-cell sequencing analysis). (**G**) Quantification of RORγ$^+$ T_{reg} cells in the cecum and colon from CTRL and Trpv1-ADC mice treated with vehicle or BIBN4096. (**H**) Quantification of RORγ$^+$ T_{reg} cells in the cecum and colon from CTRL, Trpv1-ADC- *FoxP3CreRamp1*$^{+/+}$, and Trpv1-ADC-*FoxP3CreRamp1*$^{fl/fl}$ mice. Each symbol in (A), (B), (G), and (H) represents an individual mouse; bars represent mean, and error bars are standard deviation. *P < 0.05, **P < 0.01, ***P < 0.001, and NS is no significance (unpaired Student's t test with Holm-Sidak correction for multiple comparison). Data are representative of ≥2 independent experiments. n = 4 to 10 mice per group (both male and female).

did not include most of the transcripts of the generic van Oudenaarden signature of "cell suffering" (*57*), indicating some specificity to the stress signals involved and arguing against experimental artifacts. In addition, the expression of this stress signature was more pronounced in normal mice at steady state in the targets of Trpv1 neurons, suggesting that this mode of regulation operates at baseline, independent of experimental manipulation.

Why, of the neuronal classes we probed, did Trpv1$^+$ neuron activation cause the broadest changes in immunocytes? Trpv1$^+$ neurons, as a subset of nociceptors whose primary function is to detect and transmit noxious signals to the central nervous system (CNS), are sensitized by a variety of inflammatory mediators, and nociceptors can activate the immune system through neurogenic inflammation (*63*). Correspondingly, several reports have already described isolated interactions between immunocytes and Trpv1$^+$ sensory neurons. In skin, Trpv1$^+$ neurons interact with IL-23–producing dendritic cells to drive imiquimod-induced dermatitis (*85*), and their optogenetic activation can trigger T_H17 cell responses, setting the stage for defense against fungal and bacterial pathogens (*86*). Trpv1$^+$ neurons have also been shown to have inhibitory influence over immunocytes. In bacterial skin and lung infections, Trpv1$^+$ neurons suppress neutrophil and myeloid cell responses to *Streptococcus pyogenes* and *Staphylococcus aureus* (*71*, *72*). Conversely, T_H17 cells induced by skin commensals promote sensory neuron regeneration during wound healing through IL-17 receptors on these neurons (*87*), indicating a bidirectional interface. In the gut, Trpv1$^+$ neurons mediate host defense against *Salmonella enterica* and *C. rodentium* infections (*88*, *89*). Trpv1$^+$ neurons also modulate goblet cell mucus production and microbiome homeostasis to promote gut barrier protection (*39*, *41*). The dominance of Trpv1$^+$ neurons in neuroimmune cross-talk could be consistent with the roles of both the nociceptive nervous and immune systems in monitoring the environment for danger.

Emerging evidence connects T_{reg} cell function to pain, and it is interesting to consider our results in this context. CD4$^+$ T cells, in general, may have an analgesic role; in somatic pain (*90*, *91*) and visceral pain (*92*) models, T cell depletion caused prolonged pain hypersensitivity. T_{reg} cell depletion with anti-CD25 treatment (*93*) or in Foxp3-DTR mice (*94*) led to increased mechanical hypersensitivity after sciatic nerve injury. Thus, T_{reg} cells seem to play an antinociceptive role, likely through the release of cytokines such as IL-10 and production of endogenous opioids like proenkephalin (*93*–*95*). In this work, persistent Trpv1$^+$ nociceptor activation induced a decrease of T_{reg} cells, which we speculate might represent an adaptation—the dampening of a negative feedback loop in the face of an unresolved noxious stimulus. Tight control of such nociceptor–T cell signaling may be required to prevent immunopathology. Indeed, repeated nociceptor activation led to increased susceptibility to colitis.

The circuitry of neuroimmune interactions in the gut remains a poorly understood topic. We uncovered distinct immunophenotypic changes upon neuronal activation across the intestine (ileum, cecum, colon). Several factors may affect the outcome of neuronal activation on gut immunophenotypes, including neuroanatomical innervation patterns and microbial and immunocyte compositions. Neural tracing studies have shown that vagal ganglia innervation decreases in the lower GI tract (*25*), whereas DRG spinal afferent neurons innervate the entire GI tract (*4*). Our data show that DRG, but not vagal, neurons regulate colonic and cecal T_{reg} cells. This signaling is likely through local secretion of CGRP, but we cannot rule out the possibility that Trpv1$^+$ neurons also signal through a neural reflex arc through the CNS, although not through a previously proposed vagal route (*47*). DRG sensory neurons have central terminals and reflex circuits in the spinal cord and more complex circuits in higher cortical areas. Recent work has mapped CNS regions linked to mouse models of gut inflammation, including DSS-induced colitis and food allergies (*96*–*98*). It would be interesting to determine whether such brain regions are also connected with peripheral neuron subsets that actively regulate immunity in the gut.

Overall, our study used a DREADD-based in vivo neuronal activation system to discover a number of neuroimmune interactions that control and modify immunocyte populations in the gut and demonstrate a role for Trpv1$^+$ neurons in modulating gut T_{reg} cells via CGRP-RAMP1 signaling. These observations raise the intriguing possibility that the nervous and immune systems, with their molecularly different sensory modalities, cooperate toward a balanced response to potentially noxious challenges in the digestive tract.

Materials and methods

Mice

We used aged matched 6- to 12-week-old littermate male and female mice for all experiments. C57BL/6J (B6), B6;129S6-*Chat*$^{tm2(cre)Lowl}$/J (Chat-Cre), B6.129-*Trpv1*$^{tm1(cre)Bbm}$/J (Trpv1-Cre), B6.129-*Nos1*$^{tm1(cre)Mgmj}$/J (Nos1-Cre), *Vip*$^{tm1(cre)Zjh}$/J (Vip-Cre), B6.Cg-*7630403G23Rik*$^{Tg(Th-cre)1Tmd}$/J (Th-Cre), *Mrgprd* $^{tm1.1(cre/ERT2)Wql}$/J (Mrgprd-CreER), B6;129S-*Tac1* $^{tm1.1(cre)Hze}$/J (Tac1-Cre), B6(SJL)-*Piezo2* $^{tm1.1(cre)Apat}$/J (Piezo2-Cre), B6.129 (Cg)-$^{Foxp3tm4(YFP/icre)Ayr}$/J (FoxP3-CreYFP), and B6.Cg-Tac1^{tm1Bbm}/J (*Tac1*$^{-/-}$) mice were purchased and obtained from the Jackson Laboratory (Bar Harbor, Maine) and bred in the specific-pathogen free animal facility at Harvard Medical School (HMS). B6.129S6-Calca^{tm1}Hku (*Calca*$^{-/-}$) mice were kindly provided by V. Kuchroo (HMS). Ramp1$^{tm1a(EUCOMM)Wtsi}$/H (Ramp1$^{flox/flox}$) mice were purchased from the European Mouse Mutant Archive (EMMA). Kaede transgenic (Kaede) mice were originally obtained from O. Kanagawa (RIKEN, Wako, Japan). Trpv1-Cre, Chat-Cre, Nos1-Cre, Vip-Cre, Th-Cre, Mrgprd-CreER, Tac1-Cre, and Piezo2-Cre mice were crossed with B6 mice to generate Trpv1-Cre$^{+/-}$, Chat-Cre$^{+/-}$, Nos1-Cre$^{+/-}$, Vip-Cre$^{+/-}$, Th-Cre$^{+/-}$, Mrgprd-CreER$^{+/-}$, Tac1-Cre$^{+/-}$, Piezo2-Cre$^{+/-}$, and littermate control mice to use for subsequent AAV-based experiments outlined below. For analysis of immune migration, Trpv1-Cre$^{+/-}$ mice were crossed with Kaede mice to generate Trpv1-Cre$^{+/-}$Kaede and Trpv1-Cre$^{-/-}$Kaede mice. For assays related to the role of neuropeptides in immunity, Trpv1-Cre mice were crossed with *Tac1*$^{-/-}$ or *Calca*$^{-/-}$ mice to generate Trpv1-Cre$^{+/-}$*Tac1*$^{+/-}$ or Trpv1-Cre$^{+/-}$*Calca*$^{+/-}$ mice, and F_1 heterozygotes further crossed to *Tac1*$^{+/-}$ or *Calca*$^{+/-}$ mice to generate Trpv1-Cre$^{+/-}$*Tac1*$^{-/-}$ or Trpv1-Cre$^{+/-}$*Calca*$^{-/-}$ mice and littermate controls, respectively. For T_{reg} cell–specific deletion of RAMP1, which is the co-receptor for CGRP, FoxP3-CreYFP mice were crossed with Ramp1$^{flox/flox}$ mice. FoxP3-CreYFP-Ramp1$^{flox/flox}$ mice were then crossed with Trpv1-Cre mice to generate Trpv1Cre$^{+/-}$FoxP3-CreYFP-Ramp1$^{flox/flox}$ mice.

Mice were bred and maintained in the animal facility at HMS under specific pathogen–free conditions with food and water ad libitum and a 12-hour dark-light cycle. CO_2 inhalation was used for euthanasia. All experiments with animals were approved by the HMS Institutional Animal Use and Care Committee (protocols IS00001257 and IS00000054-6).

Systemic and targeted viral DREADD expression and chemogenetic activation

For systemic AAV-mediated delivery, we used AAV.PhP.S-hSyn-DIO-hM3D(Gq)-mCherry (AAV^{hM3Dq}) to mediate Cre-dependent expression of the DREADD hM3Dq in neurons (*22*). Viruses were produced at the Boston Children's Hospital viral core facility. Neonatal pups (either Cre$^+$ or Cre$^-$ littermates) at postnatal stage 1 (P1) were injected intraperitoneally with 10 μl of AAV^{hM3Dq} at a dose of 2×10^{11} viral genomes per mouse.

For DRG-targeted AAV-mediated delivery, we used the AAV9-hSyn-DIO-hM3D(Gq)-mCherry (AAV9^{hM3Dq}). Viruses were purchased from Addgene. Ten microliters of AAV9^{hM3Dq} virus was injected intrathecally on 3 consecutive days. Mice were briefly anesthetized with isoflurane and injected in the L5-L6 region. Mice were rested for 3 to 4 weeks before being used for experiments.

For vagal ganglia–targeted expression, the NG and jugular ganglia were bilaterally injected as previously described (*60*). Briefly, adult mice

were anesthetized, and an incision was made along the ventral surface of the neck. The NG and jugular ganglia were surgically exposed by blunt dissection and a micropipette containing the virus was inserted into the NG. One hundred fifty nanoliters of AAV9^{hM3Dq} virus was injected using a Nanoinject II injector (Drummond). Mice were allowed to recover for 4 weeks before being used for experiments.

To stimulate neuronal activation in mice, 1 mg per kg body weight (mg/kg) of CNO (Tocris 4936) was injected intraperitoneally. For c-FOS experiments, mice received one injection of CNO and were sacrificed at 1.5, 7, or 24 hours after injection. Mice were administered CNO every other day for a 2-week period or consecutively for 1 day or 7 days. Mice were sacrificed the day after the last CNO injection, unless otherwise specified in the Results section of the main text.

Trpv1$^+$ DRG neuron ablation

For targeted ablation of Trpv1$^+$ DRG neurons, 4- to 6-week-old mice were intrathecally injected with RTX (Alamone labs R-400), (25 ng per mouse) or vehicle in 10 μl of 0.25% dimethyl sulfoxide (DMSO)/0.02% Tween-80/0.05% ascorbic acid/phosphate-buffered saline (PBS) in the L5-L6 region under isoflurane on two consecutive days. Control mice were injected intrathecally with vehicle alone. Mice were allowed to rest for 3 to 4 weeks before being used for experiments. We confirmed the loss of Trpv1$^+$ neurons in the DRG but not vagal ganglia by immunostaining (see section "Immunofluorescence and microscopy") or reduced thermal responses to noxious heat during hot-plate tests (55°C).

RAMP1 antagonist administration

For antagonist experiments, BIBN4096 (Tocris, 4561) was injected intraperitoneally at a dose of 0.3 mg/kg 1 hour before CNO injections.

DSS-induced colitis and C. rodentium *infection*

For DSS-induced acute colitis in mice, 2.5% DSS salt (Thermo Scientific) was dissolved in the drinking water and given to mice for 6 days, followed by normal drinking water for 4 days. Mice were monitored daily for morbidity (piloerection, lethargy), weight loss, and rectal bleeding.

For longer term DSS-induced colitis in mice, 1.5% DSS salt (Thermo Scientific) was dissolved in the drinking water and given to mice for 21 days. Mice were monitored daily for morbidity (piloerection, lethargy), weight loss, and rectal bleeding.

For *C. rodentium* infections in mice, *C. rodentium* strain DBS100 (ATCC, 51459) was used. Bacteria were grown overnight for 16 to 18 hours in Luria Bertani (LB) broth at 37°C at 250 rpm. The optical density at 600 nm (OD600) was determined to estimate bacterial density, and serial plating was performed to quantify the infection dose by counting colony forming units (CFU). Mice were fasted overnight and then orally gavaged with 200 μl of sterile PBS containing 2×10^9 CFU. Mice were monitored daily throughout the experiment. To detect *C. rodentium* colonization, fecal pellets, liver, or spleen were homogenized in 1 ml of PBS, serially diluted, and plated on MacConkey agar for counting. *C. rodentium* CFU were counted after overnight incubation at 37°C.

Photoconversion procedures

Colon was photoconverted as previously described (*54*). Briefly, a custom-built fiberoptic endoscope (ZIBRA Corporation) was coupled to a handheld 405-nm blue purple laser (≤5 mW) by an in-house custom-made connection device (fixed mounts from ThorLabs). Mice were anesthetized with ketamine:xylazine (10 mg/kg: 2 mg/kg intraperitoneally). After cleansing the colon of fecal pellets with PBS, the fiberoptic endoscope was inserted through the anus to a depth of 3 cm. The laser was switched on, exposing the inner colon to violet light (3.5-mm beam diameter). Subsequently, the endoscope was gently retracted, pausing at 2-mm increments for 30-s light pulses at each interval (for a total of up to 10 min).

Immunocyte isolation from tissues

Spleen

Single-cell suspensions were prepared by mashing the splenic tissue through a 70-μm cell strainer followed by washing in RPMI containing 5% fetal calf serum (FCS). Red blood cells in the spleen were lysed with ACK lysing buffer (Gibco, ref. A10492-01).

mLNs

mLNs were minced into small pieces and dissociated in collagenase solution [1 mg/ml collagenase VIII (Sigma), 0.1 mg/ml DNase I (Sigma), and 2% FCS in RPMI] with constant shaking at 37°C for 30 min. Single-cell suspensions were filtered through a 40-μm cell strainer and washed with RPMI containing 5% FCS.

Ileum, cecum, and colon

Intestines were cleaned (Peyer's patches were removed in the case of the ileum) and treated with RPMI containing 1 mM dithiothreitol (DTT), 20 mM EDTA, and 2% FCS at 37°C for 15 min to remove epithelial cells. Tissues were then minced and dissociated in collagenase solution [1.5 mg/ml collagenase II (Gibco), 0.5mg/ml dispase (Gibco) and 1% FCS in RPMI] with constant stirring at 37°C for 40 min. Single-cell suspensions were filtered through a 40-μm cell strainer and washed with RPMI containing 5% FCS.

Flow cytometry

Single-cell suspensions from spleen and intestinal tissues were prepared as above. The cells were stained with two constant panels of antibodies for consistency. The first panel (lymphoid panel) included surface markers for CD19, CD4, CD8a, CD8b, TCR-β, TCR-γδ, NK1.1, CD138, and CD44 and intracellular markers for RORγ, FoxP3, Tbet, Gata3, and Helios. The second panel (myeloid panel) included surface markers for CD45, CD19, CD11b, CD11c, Ly6c, Ly6g, PDCA-1, F4/80, CD103, and MHCII. The Thetis or Janus cell-staining panel included surface markers for CD45, TCR-β, TCR-γδ, B220, CD11c, CD127, MHCII, CCR6, and CXCR6 and intracellular markers for RORγ and FoxP3. The cells were stained with zombie live-dead dye (BioLegend) at 4°C for 20 min, followed by surface staining at 4°C for 30 min. For intracellular staining, cells were fixed in eBioscience Fix/Perm buffer at room temperature for 1 hour, followed by permeabilization in eBioscience permeabilization buffer at room temperature for 1 hour in the presence of antibodies. For Annexin-V staining, the cells were stained with antibody for Annexin-V in Annexin-V binding buffer at room temperature for 10 min after surface staining. Cells were acquired with a Symphony flow cytometer (BD Biosciences) and analysis was performed with FlowJo (Tree Star) software. The antibody information can be found in data S7.

Whole-mount staining

Mice were euthanized, and a small piece (3 mm by 3 mm) of distal colon was collected for staining. The colons were opened and fixed in a Silgard dish with 4% paraformaldehyde (PFA) at 4°C for 2 hours. Then, the tissues were washed with PBST (PBS with 0.5% Triton-X100) six times at room temperature for 20 min, followed by incubation with primary antibodies (Tuj1 and mCherry, or CGRP and FoxP3) in blocking buffer (20% DMSO, 5% donkey serum or goat serum in PBST) for 2 to 3 days and corresponding secondary antibodies in blocking buffer for 1 to 2 days. In subsets of experiments, tissue was dehydrated with serial (50, 80, and 100%) methanol solution and cleared in BABB buffer (1 volume benzyl alcohol to 2 volume benzyl benzoate). The tissues were mounted on glass slides using vacuum grease for imaging. Three different fields of each tissue were imaged by Ti2 Spinning Disk microscope (Nikon) or a Stellaris 8 FALCON CFS system (Leica) and processed by ImageJ software. All images were maximum intensity projections of z-stacks. For quantification of the myenteric plexus in whole-mount colon images, the percentage of mCherry$^+$ area out of total Tuj1$^+$ area was determined for each sample as an average of two fields per mouse and quantified by investigators blinded to genotypes.

Immunofluorescence and microscopy

For immunostaining of extrinsic ganglia, tissues were placed in 4% PFA for 1 to 2 hours.

For immunostaining of spinal cord, tissues were placed in 4% PFA for 4 to 6 hours. Thoracic (T11-T13) DRG and spinal cord, lumbar (L5-L6) DRG and spinal cord, and vagal ganglia were dissected, incubated overnight at 4°C in 30% sucrose, and embedded in OCT compound (SAKURA). Sections (14 μm for DRG, 25 μm for spinal cord) were cut, blocked with 10% normal donkey serum (NDS) and 0.05% Tween-20 in PBS for 2 hours at room temperature, and stained with primary antibodies (goat anti-mCherry, rabbit anti-Tuj1, or goat anti-mCherry and rabbit anti-cFOS) overnight at room temperature. Sections were washed in PBS and then stained with secondary antibodies (donkey anti-goat Alexa594, donkey anti-rabbit Alexa488) for 2 hours at room temperature. After washing with PBS, sections were mounted in VectaShield (Vector Labs). Sections were imaged on a Leica Stellaris 8 FALCON CFS confocal microscope at 20× magnification. Leica software (Leica Application Suite X) was used for image capture and postprocessing. For quantification of extrinsic ganglia neurons, the percentage of mCherry$^+$ neurons out of the total Tuj1$^+$ neurons were determined for each sample as an average of 3 to 5 fields per mouse and quantified by investigators were blinded to genotypes. For quantification of spinal cord cells, the total number of c-FOS–positive cells in the dorsal horn were counted in four sections per mouse and quantified by investigators blinded to genotypes.

Quantification of T_{reg} cell distance to nearest nerve fiber

Quantification of the distance from FoxP3$^+$ T_{reg} cells to the nearest CGRP$^+$ nerve fibers were performed using ImageJ. T_{reg} cells and nerve fibers were detected by local thresholding, after which nerve fibers were skeletonized. The distance of each T_{reg} cell to each point on all nerve fibers was computed to identify the distance of the cells from the closest point of the nearest nerve fiber. This method of analyzing distances of cells to the closest nerve fiber was repeated on multiple optical sections of whole-mount colon tissue. Each optical section analyzed was spaced at least 200 μm away from the previous section to avoid overlap of the same cells. The graphs summarize quantifications obtained from five mice, with two sections of whole-mount colon tissue from each mouse.

For randomization analysis, the same experimental slices were reanalyzed. In this case, in each optical section, after detection of the cells, the same number of cells were randomly distributed in the image by a random number generator. The closest distance of the cells to the nerve fibers was subsequently computed as described previously. The frequency distribution and nonlinear regression analysis were done through GraphPad Prism.

Gut histopathology

Mice were euthanized, and colon tissues were collected and fixed in 10% formalin for at least 24 hours before hematoxylin and eosin (H&E) staining. Whole cross sections were scanned and imaged on a widefield microscope (Nikon) at either 10× or 20× magnification. To evaluate inflammation, H&E-stained sections were randomly split into eight sections, and four random sections were scored qualitatively using a 0- to 5-point scale for immune infiltrate, goblet cell loss, crypt density, crypt hyperplasia, muscle thickening, submucosal infiltrate, ulceration, and abscess. Scores from each item were combined for a composite score for each mouse. Scores from each section were averaged for each mouse. Scoring was performed blinded.

Fecal DNA extraction, 16S rDNA sequencing, and data analysis

Feces from colons were collected and frozen at −80°C until use. Bacterial genomic DNA from fecal samples was extracted using phenol: chloroform:isoamyl alcohol and purified with the QIAquick PCR Purification kit (Qiagen). Purified DNA was quantified by Qubit dsDNA HS Assay (Thermo Fisher) and normalized to 6 ng/μl for amplification. Amplicons were quantified by Qubit dsDNA HS Assay and combined with equal mass to make a pooled library. The pooled library was purified and multiplexed sequenced (Illumina MiSeq, 251 nucleotides times 2 pair-end reads with 12-nucleotide index reads) through Harvard's Biopolymers Facility. Raw sequencing data were processed with QIIME2. In brief, raw sequencing data were imported to QIIME2 and demultiplexed, and then DADA2 was used for sequence quality control and feature table construction. The feature table was used for beta diversity analysis, taxonomic analysis, and differential abundance testing using QIIME2. Beta group significance was determined by permutational analysis of variance (PERMANOVA). Identification of taxa associated with different groups was determined using analysis of composition of microbiomes (ANCOM).

scRNA-seq and data analysis

Sample preparation and sequencing

scRNA-seq experiments were performed and analyzed as previously described (*99*). Cecum cell suspensions were stained with surface markers for CD45, CD4, CD19, CD8a, CD11b, CD11c, TCR-γδ, NK1.1, and 4′,6-diamidino-2-phenylindole (DAPI) as a viability dye, along with hashtag antibodies (hashtag 1, CTRL#1; hashtag 3, CTRL#2; hashtag 7, Trpv1-ADC#1; hashtag 9, Trpv1-ADC#2). Cells were sorted as DAPI$^-$CD45$^+$. Additional sorting was performed for CD19$^-$CD45$^+$, NK1.1$^+$CD45$^+$, and TCR-γδ $^+$CD45$^+$ to enrich for these populations. All samples were pooled together, centrifuged, and resuspended in 0.04% bovine serum albumin (BSA). Encapsulation was done on the 10X Chromium microfluidic instrument (10X Genomics). Libraries were prepared using Chromium Single Cell 3′ Reagents Kit v2 according to the manufacturer's protocol. Libraries were sequenced together on the Illumina HiSeq X.

Data analysis

scRNA-seq data were processed using the standard CellRanger pipeline (10X Genomics). Hashtag oligo (HTO) counts were obtained using the CITE-seq-Count package. Data were analyzed in R using the Seurat package (*100*). HTOs were assigned to cells using the HTODemux function, and doublets were eliminated from analysis. Cells with fewer than 700 unique molecular identifiers (UMIs) or 500 genes and more than 2500 UMIs, 10,000 genes, and 5% of reads mapped to mitochondrial genes were also excluded from the analysis. Dimensionality reduction, visualization, and clustering analysis were performed in Seurat using the NormalizeData, ScaleData, FindVariableGenes, RunPCA, FindNeighbors (dims=1:30), RunUMAP (dims=1:30), and FindClusters functions. Cluster identity was determined based on expression of key marker genes (fig. S8A). The SubsetData function was used to gate individual clusters for further analysis.

Differentially expressed genes (DEGs) between Trpv1-ADC and CTRL mice were obtained using the FindMarkers function, with the cutoff based on fold change and *P* value (logfc.threshold = 0.5 and adjusted *P* value <0.05) on seven populations including CD4$^+$ T_{conv} cells (T4conv), CD4$^+$ T_{reg} cells (Treg), CD8a$^+$ CD8b$^+$ T cells (T8ab), CD160$^+$ IEL (IEL-like), B cells (B), ILCs (ILC), and selected myeloid cells (macrophage and dendritic cells, MacDC), respectively. Then, the DEGs from each population were collated nonredundantly. The average expression of these DEGs in each sample (two pairs of Trpv1-ADC and CTRL mice) across each population were generated using AverageExpression function. Heatmaps of DEGs were generated using Morpheus (Broad Institute).

Gene signatures

The IEL gene signature was based on the expression of the following marker genes: *Klra1*, *Klre1*, *Klra7*, *Itgae*, *Cd160*, *Klrk1*, *Fasl*, *Itgb7*, *Ccr9*, and *Cd8a*. The Helios T_{reg} cell gene signature was based on the expression of the following marker genes: *Cd200r1*, *Cd83*, *Dgat2*, *Epas1*, *Fam46a*, *Gas2l3*, *Ikzf2*, *Il9r*, *Naip5*, *Nrp1*, *Ppp2r3a*, *Swap70*, and *Foxp3*. The *Rorc* T_{reg} cell gene signature was based on the expression of the following marker genes: *Ccr1*, *Ccr2*, *Ccr5*, *Ccr9*, *Clic4*, *F2rl2*, *Gpr15*, *Havcr2*, *Itgb5*, *Marcks*, *Matn2*, *Nr1d1*, *Prg4*, and *Rorc*.

Data analysis and statistics

Data are represented as mean and standard deviation, where *n* represents the number of

mice, unless indicated otherwise. Statistical tests used were unpaired Student's *t* test with Holm-Sidak correction for multiple comparison or two-way repeated measures ANOVA, as indicated in the figure legends. Differences were considered significant if $P < 0.05$. Statistics were performed in GraphPad Prism.

REFERENCES AND NOTES

1. A. Jacobson, D. Yang, M. Vella, I. M. Chiu, The intestinal neuro-immune axis: Crosstalk between neurons, immune cells, and microbes. *Mucosal Immunol.* **14**, 555–565 (2021). doi: 10.1038/s41385-020-00368-1; pmid: 33542493
2. H. Wang, J. P. P. Foong, N. L. Harris, J. C. Bornstein, Enteric neuroimmune interactions coordinate intestinal responses in health and disease. *Mucosal Immunol.* **15**, 27–39 (2022). doi: 10.1038/s41385-021-00443-1; pmid: 34471248
3. J. F. Cryan, T. G. Dinan, Gut microbiota: Microbiota and neuroimmune signalling—Metchnikoff to microglia. *Nat. Rev. Gastroenterol. Hepatol.* **12**, 494–496 (2015). doi: 10.1038/nrgastro.2015.127; pmid: 26215386
4. L. A. Blackshaw, S. J. Brookes, D. Grundy, M. Schemann, Sensory transmission in the gastrointestinal tract. *Neurogastroenterol. Motil.* **19**, 1–19 (2007). doi: 10.1111/j.1365-2982.2006.00871.x; pmid: 17280582
5. M. Costa, S. J. Brookes, G. W. Hennig, Anatomy and physiology of the enteric nervous system. *Gut* **47**, iv15–iv19 (2000). doi: 10.1136/gut.47.suppl_4.iv15; pmid: 11076898
6. L. K. McCorry, Physiology of the autonomic nervous ystem. *Am. J. Pharm. Educ.* **71**, 78 (2007). doi: 10.5688/aj710478; pmid: 17786266
7. A. Zeisel *et al*., Molecular architecture of the mouse nervous system. *Cell* **174**, 999–1014.e22 (2018). doi: 10.1016/j.cell.2018.06.021; pmid: 30096314
8. J. R. F. Hockley *et al*., Single-cell RNAseq reveals seven classes of colonic sensory neuron. *Gut* **68**, 633–644 (2019). doi: 10.1136/gutjnl-2017-315631; pmid: 29483303
9. J. Kupari, M. Häring, E. Agirre, G. Castelo-Branco, P. Ernfors, An atlas of vagal sensory neurons and their molecular specialization. *Cell Rep.* **27**, 2508–2523.e4 (2019). doi: 10.1016/j.celrep.2019.04.096; pmid: 31116992
10. J. Talbot *et al*., Feeding-dependent VIP neuron-ILC3 circuit regulates the intestinal barrier. *Nature* **579**, 575–580 (2020). doi: 10.1038/s41586-020-2039-9; pmid: 32050257
11. C. Seillet *et al*., The neuropeptide VIP confers anticipatory mucosal immunity by regulating ILC3 activity. *Nat. Immunol.* **21**, 168–177 (2020). doi: 10.1038/s41590-019-0567-y; pmid: 31873294
12. M. Pascal *et al*., The neuropeptide VIP potentiates intestinal innate type 2 and type 3 immunity in response to feeding. *Mucosal Immunol.* **15**, 629–641 (2022). doi: 10.1038/s41385-022-00516-9; pmid: 35501356
13. A. Wallrapp *et al*., The neuropeptide NMU amplifies ILC2-driven allergic lung inflammation. *Nature* **549**, 351–356 (2017). doi: 10.1038/nature24029; pmid: 28902842
14. V. Cardoso *et al*., Neuronal regulation of type 2 innate lymphoid cells via neuromedin U. *Nature* **549**, 277–281 (2017). doi: 10.1038/nature23469; pmid: 28869974
15. C. S. N. Klose *et al*., The neuropeptide neuromedin U stimulates innate lymphoid cells and type 2 inflammation. *Nature* **549**, 282–286 (2017). doi: 10.1038/nature23676; pmid: 28869965
16. I. Gabanyi *et al*., Neuro-immune interactions drive tissue programming in intestinal macrophages. *Cell* **164**, 378–391 (2016). doi: 10.1016/j.cell.2015.12.023; pmid: 26777404
17. F. Matheis *et al*., Adrenergic signaling in muscularis macrophages limits infection-induced neuronal loss. *Cell* **180**, 64–78.e16 (2020). doi: 10.1016/j.cell.2019.12.002; pmid: 31923400
18. S. Moriyama *et al*., β_2-adrenergic receptor-mediated negative regulation of group 2 innate lymphoid cell responses. *Science* **359**, 1056–1061 (2018). doi: 10.1126/science.aan4829; pmid: 29496881
19. D. J. Urban, B. L. Roth, DREADDs (designer receptors exclusively activated by designer drugs): Chemogenetic tools with therapeutic utility. *Annu. Rev. Pharmacol. Toxicol.* **55**, 399–417 (2015). doi: 10.1146/annurev-pharmtox-010814-124803; pmid: 25292433
20. D. Atasoy, J. N. Betley, H. H. Su, S. M. Sternson, Deconstruction of a neural circuit for hunger. *Nature* **488**, 172–177 (2012). doi: 10.1038/nature11270; pmid: 22801496
21. E. S. Yoo *et al*., $G\alpha_{i/o}$-coupled *Htr2c* in the paraventricular nucleus of the hypothalamus antagonizes the anorectic effect of serotonin agents. *Cell Rep.* **37**, 109997 (2021). doi: 10.1016/j.celrep.2021.109997; pmid: 34788630
22. K. Y. Chan *et al*., Engineered AAVs for efficient noninvasive gene delivery to the central and peripheral nervous systems. *Nat. Neurosci.* **20**, 1172–1179 (2017). doi: 10.1038/nn.4593; pmid: 28671695
23. B. N. Armbruster, X. Li, M. H. Pausch, S. Herlitze, B. L. Roth, Evolving the lock to fit the key to create a family of G protein-coupled receptors potently activated by an inert ligand. *Proc. Natl. Acad. Sci. U.S.A.* **104**, 5163–5168 (2007). doi: 10.1073/pnas.0700293104; pmid: 17360345
24. T. Ogura *et al*., Utility of intraperitoneal administration as a route of AAV serotype 5 vector-mediated neonatal gene transfer. *J. Gene Med.* **8**, 990–997 (2006). doi: 10.1002/jgm.916; pmid: 16685745
25. R. J. Phillips, T. L. Powley, Innervation of the gastrointestinal tract: Patterns of aging. *Auton. Neurosci.* **136**, 1–19 (2007). doi: 10.1016/j.autneu.2007.04.005; pmid: 17537681
26. T. Uesaka, H. M. Young, V. Pachnis, H. Enomoto, Development of the intrinsic and extrinsic innervation of the gut. *Dev. Biol.* **417**, 158–167 (2016). doi: 10.1016/j.ydbio.2016.04.016; pmid: 27112528
27. S. H. Woo *et al*., Piezo2 is required for Merkel-cell mechanotransduction. *Nature* **509**, 622–626 (2014). doi: 10.1038/nature13251; pmid: 24717433
28. J. A. Harris *et al*., Anatomical characterization of Cre driver mice for neural circuit mapping and manipulation. *Front. Neural Circuits* **8**, 76 (2014). doi: 10.3389/fncir.2014.00076; pmid: 25071457
29. W. Olson *et al*., Sparse genetic tracing reveals regionally specific functional organization of mammalian nociceptors. *eLife* **6**, e29507 (2017). doi: 10.7554/eLife.29507; pmid: 29022879
30. J. M. Savitt, S. S. Jang, W. Mu, V. L. Dawson, T. M. Dawson, Bcl-x is required for proper development of the mouse substantia nigra. *J. Neurosci.* **25**, 6721–6728 (2005). doi: 10.1523/JNEUROSCI.0760-05.2005; pmid: 16033881
31. D. J. Cavanaugh *et al*., Trpv1 reporter mice reveal highly restricted brain distribution and functional expression in arteriolar smooth muscle cells. *J. Neurosci.* **31**, 5067–5077 (2011). doi: 10.1523/JNEUROSCI.6451-10.2011; pmid: 21451044
32. J. Rossi *et al*., Melanocortin-4 receptors expressed by cholinergic neurons regulate energy balance and glucose homeostasis. *Cell Metab.* **13**, 195–204 (2011). doi: 10.1016/j.cmet.2011.01.010; pmid: 21284986
33. R. L. Leshan, M. Greenwald-Yarnell, C. M. Patterson, I. E. Gonzalez, M. G. Myers Jr., Leptin action through hypothalamic nitric oxide synthase-1-expressing neurons controls energy balance. *Nat. Med.* **18**, 820–823 (2012). doi: 10.1038/nm.2724; pmid: 22522563
34. H. Taniguchi *et al*., A resource of Cre driver lines for genetic targeting of GABAergic neurons in cerebral cortex. *Neuron* **71**, 995–1013 (2011). doi: 10.1016/j.neuron.2011.07.026; pmid: 21943598
35. G. M. Alexander *et al*., Remote control of neuronal activity in transgenic mice expressing evolved G protein-coupled receptors. *Neuron* **63**, 27–39 (2009). doi: 10.1016/j.neuron.2009.06.014; pmid: 19607790
36. M. Jendryka *et al*., Pharmacokinetic and pharmacodynamic actions of clozapine-N-oxide, clozapine, and compound 21 in DREADD-based chemogenetics in mice. *Sci. Rep.* **9**, 4522 (2019). doi: 10.1038/s41598-019-41088-2; pmid: 30872749
37. M. D. Gershon, K. G. Margolis, The gut, its microbiome, and the brain: Connections and communications. *J. Clin. Invest.* **131**, e143768 (2021). doi: 10.1172/JCI143768; pmid: 34523615
38. J. F. Cryan *et al*., The microbiota-gut-brain axis. *Physiol. Rev.* **99**, 1877–2013 (2019). doi: 10.1152/physrev.00018.2018; pmid: 31460832
39. D. Yang *et al*., Nociceptor neurons direct goblet cells via a CGRP-RAMP1 axis to drive mucus production and gut barrier protection. *Cell* **185**, 4190–4205.e25 (2022). doi: 10.1016/j.cell.2022.09.024; pmid: 36243004
40. W. Zhang *et al*., Gut-innervating nociceptors regulate the intestinal microbiota to promote tissue protection. *Cell* **185**, 4170–4189.e20 (2022). doi: 10.1016/j.cell.2022.09.008; pmid: 36240781
41. E. Sefik *et al*., Individual intestinal symbionts induce a distinct population of $ROR\gamma^+$ regulatory T cells. *Science* **349**, 993–997 (2015). doi: 10.1126/science.aaa9420; pmid: 26272906
42. M. J. Caterina *et al*., The capsaicin receptor: A heat-activated ion channel in the pain pathway. *Nature* **389**, 816–824 (1997). doi: 10.1038/39807; pmid: 9349813
43. D. Ramanan *et al*., Regulatory T cells in the face of the intestinal microbiota. *Nat. Rev. Immunol.* **23**, 749–762 (2023). doi: 10.1038/s41577-023-00890-w; pmid: 37316560
44. B. R. Traxinger, L. E. Richert-Spuhler, J. M. Lund, Mucosal tissue regulatory T cells are integral in balancing immunity and tolerance at portals of antigen entry. *Mucosal Immunol.* **15**, 398–407 (2022). doi: 10.1038/s41385-021-00471-x; pmid: 34845322
45. N. Yissachar *et al*., An intestinal organ culture system uncovers a role for the nervous system in microbe-immune crosstalk. *Cell* **168**, 1135–1148.e12 (2017). doi: 10.1016/j.cell.2017.02.009; pmid: 28262351
46. Y. Yan *et al*., Interleukin-6 produced by enteric neurons regulates the number and phenotype of microbe-responsive regulatory T cells in the gut. *Immunity* **54**, 499–513.e5 (2021). doi: 10.1016/j.immuni.2021.02.002; pmid: 33691135
47. T. Teratani *et al*., The liver-brain-gut neural arc maintains the T_{reg} cell niche in the gut. *Nature* **585**, 591–596 (2020). doi: 10.1038/s41586-020-2425-3; pmid: 32526765
48. S. Galván-Peña, Y. Zhu, D. Mathis, C. Benoist, A dynamic atlas of immunocyte migration from the gut. *Sci. Immunol.* **9**, eadi0672 (2022). doi: 10.1126/science.aaa9420; pmid: 26272906
49. B. S. Hanna *et al*., The gut microbiota promotes distal tissue regeneration via $ROR\gamma^+$ regulatory T cell emissaries. *Immunity* **56**, 829–846.e8 (2023). doi: 10.1016/j.immuni.2023.01.033; pmid: 36822206
50. K. Chowdhary, J. Léon, D. Ramanan, D. Mathis, C. Benoist, An interwoven network of transcription factors, with divergent influences from FoxP3, underlies Treg diversity. bioRxiv 2023.05.18.541358 [Preprint] (2023); https://doi.org/10.1101/2023.05.18.541358.
51. R. Kedmi *et al*., A $ROR\gamma t^+$ cell instructs gut microbiota-specific T_{reg} cell differentiation. *Nature* **610**, 737–743 (2022). doi: 10.1038/s41586-022-05089-y; pmid: 36071167
52. B. Akagbosu *et al*., Novel antigen-presenting cell imparts T_{reg}-dependent tolerance to gut microbiota. *Nature* **610**, 752–760 (2022). doi: 10.1038/s41586-022-05309-5; pmid: 36070798
53. M. Tomura *et al*., Monitoring cellular movement in vivo with photoconvertible fluorescence protein "Kaede" transgenic mice. *Proc. Natl. Acad. Sci. U.S.A.* **105**, 10871–10876 (2008). doi: 10.1073/pnas.0802278105; pmid: 18663225
54. A. M. Morton *et al*., Endoscopic photoconversion reveals unexpectedly broad leukocyte trafficking to and from the gut. *Proc. Natl. Acad. Sci. U.S.A.* **111**, 6696–6701 (2014). doi: 10.1073/pnas.1405634111; pmid: 24753589
55. I. Miller *et al*., Ki67 is a graded rather than a binary marker of proliferation versus quiescence. *Cell Rep.* **24**, 1105–1112.e5 (2018). doi: 10.1016/j.celrep.2018.06.110; pmid: 30067968
56. V. F. Crepin, J. W. Collins, M. Habibzay, G. Frankel, *Citrobacter rodentium* mouse model of bacterial infection. *Nat. Protoc.* **11**, 1851–1876 (2016). doi: 10.1038/nprot.2016.100; pmid: 27606775
57. S. C. van den Brink *et al*., Single-cell sequencing reveals dissociation-induced gene expression in tissue subpopulations. *Nat. Methods* **14**, 935–936 (2017). doi: 10.1038/nmeth.4437; pmid: 28960196
58. D. Ramanan *et al*., Homeostatic, repertoire and transcriptional relationships between colon T regulatory cell subsets. *Proc. Natl. Acad. Sci. U.S.A.* **120**, e2311566120 (2023). doi: 10.1073/pnas.2311566120; pmid: 38064511
59. A. G. J. Skorput *et al*., Targeting the somatosensory system with AAV9 and AAV2retro viral vectors. *PLOS ONE* **17**, e0264938 (2022). doi: 10.1371/journal.pone.0264938; pmid: 35271639
60. R. B. Chang, D. E. Strochlic, E. K. Williams, B. D. Umans, S. D. Liberles, Vagal sensory neuron subtypes that differentially control breathing. *Cell* **161**, 622–633 (2015). doi: 10.1016/j.cell.2015.03.022; pmid: 25892222
61. S. K. Mishra, M. A. Hoon, Ablation of TrpV1 neurons reveals their selective role in thermal pain sensation. *Mol. Cell. Neurosci.* **43**, 157–163 (2010). doi: 10.1016/j.mcn.2009.10.006; pmid: 19853036
62. T. J. Price, C. M. Flores, Critical evaluation of the colocalization between calcitonin gene-related peptide, substance P, transient receptor potential vanilloid subfamily type 1 immunoreactivities, and isolectin B4 binding in primary afferent neurons of the rat and mouse. *J. Pain* **8**, 263–272 (2007). doi: 10.1016/j.jpain.2006.09.005; pmid: 17113352

63. I. M. Chiu, C. A. von Hehn, C. J. Woolf, Neurogenic inflammation and the peripheral nervous system in host defense and immunopathology. *Nat. Neurosci.* **15**, 1063–1067 (2012). doi: 10.1038/nn.3144; pmid: 22837035
64. Y. Q. Cao *et al*., Primary afferent tachykinins are required to experience moderate to intense pain. *Nature* **392**, 390–394 (1998). doi: 10.1038/32897; pmid: 9537322
65. F. A. Russell, R. King, S.-J. Smillie, X. Kodji, S. D. Brain, Calcitonin gene-related peptide: Physiology and pathophysiology. *Physiol. Rev.* **94**, 1099–1142 (2014). doi: 10.1152/physrev.00034.2013; pmid: 25287861
66. B. M. Assas, J. I. Pennock, J. A. Miyan, Calcitonin gene-related peptide is a key neurotransmitter in the neuro-immune axis. *Front. Neurosci.* **8**, 23 (2014). doi: 10.3389/fnins.2014.00023; pmid: 24592205
67. P. Baral, S. Udit, I. M. Chiu, Pain and immunity: Implications for host defence. *Nat. Rev. Immunol.* **19**, 433–447 (2019). doi: 10.1038/s41577-019-0147-2; pmid: 30874629
68. H. Nagashima *et al*., Neuropeptide CGRP limits group 2 innate lymphoid cell responses and constrains type 2 inflammation. *Immunity* **51**, 682–695.e6 (2019). doi: 10.1016/j.immuni.2019.06.009; pmid: 31353223
69. A. Wallrapp *et al*., Calcitonin gene-related peptide negatively regulates alarmin-driven type 2 innate lymphoid cell responses. *Immunity* **51**, 709–723.e6 (2019). doi: 10.1016/j.immuni.2019.09.005; pmid: 31604686
70. H. Xu *et al*., Transcriptional atlas of intestinal immune cells reveals that neuropeptide α-CGRP modulates group 2 innate lymphoid cell responses. *Immunity* **51**, 696–708.e9 (2019). doi: 10.1016/j.immuni.2019.09.004; pmid: 31618654
71. F. A. Pinho-Ribeiro *et al*., Blocking neuronal signaling to immune cells treats streptococcal invasive infection. *Cell* **173**, 1083–1097.e22 (2018). doi: 10.1016/j.cell.2018.04.006; pmid: 29754819
72. P. Baral *et al*., Nociceptor sensory neurons suppress neutrophil and γδ T cell responses in bacterial lung infections and lethal pneumonia. *Nat. Med.* **24**, 417–426 (2018). doi: 10.1038/nm.4501; pmid: 29505031
73. P. Hanč *et al*., Multimodal control of dendritic cell functions by nociceptors. *Science* **379**, eabm5658 (2023). doi: 10.1126/science.abm5658; pmid: 36996219
74. K. Wang *et al*., Neuronal, stromal, and T-regulatory cell crosstalk in murine skeletal muscle. *Proc. Natl. Acad. Sci. U.S.A.* **117**, 5402–5408 (2020). doi: 10.1073/pnas.1922559117; pmid: 32102913
75. P. S. Miller *et al*., Non-peptidic antagonists of the CGRP receptor, BIBN4096BS and MK-0974, interact with the calcitonin receptor-like receptor via methionine-42 and RAMP1 via tryptophan-74. *Biochem. Biophys. Res. Commun.* **391**, 437–442 (2010). doi: 10.1016/j.bbrc.2009.11.076; pmid: 19914210
76. G. Matteoli *et al*., A distinct vagal anti-inflammatory pathway modulates intestinal muscularis resident macrophages independent of the spleen. *Gut* **63**, 938–948 (2014). doi: 10.1136/gutjnl-2013-304676; pmid: 23929694
77. P. A. Muller *et al*., Crosstalk between muscularis macrophages and enteric neurons regulates gastrointestinal motility. *Cell* **158**, 300–313 (2014). doi: 10.1016/j.cell.2014.04.050; pmid: 25036630
78. J. Dalli, R. A. Colas, H. Arnardottir, C. N. Serhan, Vagal regulation of group 3 innate lymphoid cells and the immunoresolvent PCTR1 controls infection resolution. *Immunity* **46**, 92–105 (2017). doi: 10.1016/j.immuni.2016.12.009; pmid: 28065837
79. R. Kuner, T. Kuner, Cellular circuits in the brain and their modulation in acute and chronic pain. *Physiol. Rev.* **101**, 213–258 (2021). doi: 10.1152/physrev.00040.2019; pmid: 32525759
80. M. W. Kay, V. Jain, G. Panjrath, D. Mendelowitz, Targeting parasympathetic activity to improve autonomic tone and clinical outcomes. *Physiology* **37**, 39–45 (2022). doi: 10.1152/physiol.00023.2021; pmid: 34486396
81. R. Singh, H. Zogg, U. C. Ghoshal, S. Ro, Current treatment options and therapeutic insights for gastrointestinal dysmotility and functional gastrointestinal disorders. *Front. Pharmacol.* **13**, 808195 (2022). doi: 10.3389/fphar.2022.808195; pmid: 35145413
82. N. Bódi, Z. Szalai, M. Bagyánszki, Nitrergic enteric neurons in health and disease-focus on animal models. *Int. J. Mol. Sci.* **20**, 2003 (2019). doi: 10.3390/ijms20082003; pmid: 31022832
83. K. J. Tracey, The inflammatory reflex. *Nature* **420**, 853–859 (2002). doi: 10.1038/nature01321; pmid: 12490958
84. S. Zhang *et al*., Nonpeptidergic neurons suppress mast cells via glutamate to maintain skin homeostasis. *Cell* **184**, 2151–2166.e16 (2021). doi: 10.1016/j.cell.2021.03.002; pmid: 33765440
85. L. Riol-Blanco *et al*., Nociceptive sensory neurons drive interleukin-23-mediated psoriasiform skin inflammation. *Nature* **510**, 157–161 (2014). doi: 10.1038/nature13199; pmid: 24759321
86. J. A. Cohen *et al*., Cutaneous TRPV1$^+$ neurons trigger protective innate type 17 anticipatory immunity. *Cell* **178**, 919–932.e14 (2019). doi: 10.1016/j.cell.2019.06.022; pmid: 31353219
87. M. Enamorado *et al*., Immunity to the microbiota promotes sensory neuron regeneration. *Cell* **186**, 607–620.e17 (2023). doi: 10.1016/j.cell.2022.12.037; pmid: 36640762
88. N. Y. Lai *et al*., Gut-innervating nociceptor neurons regulate Peyer's patch microfold cells and SFB levels to mediate *Salmonella* host defense. *Cell* **180**, 33–49.e22 (2020). doi: 10.1016/j.cell.2019.11.014; pmid: 31813624
89. V. T. Ramirez *et al*., Sensory nociceptive neurons contribute to host protection during enteric infection with *Citrobacter rodentium*. *J. Infect. Dis.* **221**, 1978–1988 (2020). doi: 10.1093/infdis/jiaa014; pmid: 31960920
90. K. Krukowski *et al*., CD8$^+$ T cells and endogenous IL-10 are required for resolution of chemotherapy-induced neuropathic pain. *J. Neurosci.* **36**, 11074–11083 (2016). doi: 10.1523/JNEUROSCI.3708-15.2016; pmid: 27798187
91. L. Basso *et al*., Endogenous analgesia mediated by CD4$^+$ T lymphocytes is dependent on enkephalins in mice. *J. Neuroinflammation* **13**, 132 (2016). doi: 10.1186/s12974-016-0591-x; pmid: 27245576
92. J. Boué *et al*., Endogenous regulation of visceral pain via production of opioids by colitogenic CD4$^+$ T cells in mice. *Gastroenterology* **146**, 166–175 (2014). doi: 10.1053/j.gastro.2013.09.020; pmid: 24055279
93. P. J. Austin, C. F. Kim, C. J. Perera, G. Moalem-Taylor, Regulatory T cells attenuate neuropathic pain following peripheral nerve injury and experimental autoimmune neuritis. *Pain* **153**, 1916–1931 (2012). doi: 10.1016/j.pain.2012.06.005; pmid: 22789131
94. J. G. Lees, S. S. Duffy, C. J. Perera, G. Moalem-Taylor, Depletion of Foxp3$^+$ regulatory T cells increases severity of mechanical allodynia and significantly alters systemic cytokine levels following peripheral nerve injury. *Cytokine* **71**, 207–214 (2015). doi: 10.1016/j.cyto.2014.10.028; pmid: 25461400
95. S. S. Duffy *et al*., Regulatory T cells and their derived cytokine, Interleukin-35, reduce pain in experimental autoimmune encephalomyelitis. *J. Neurosci.* **39**, 2326–2346 (2019). doi: 10.1523/JNEUROSCI.1815-18.2019; pmid: 30651334
96. T. Koren *et al*., Insular cortex neurons encode and retrieve specific immune responses. *Cell* **184**, 5902–5915.e17 (2021). doi: 10.1016/j.cell.2021.10.013; pmid: 34752731
97. E. B. Florsheim *et al*., Immune sensing of food allergens promotes avoidance behaviour. *Nature* **620**, 643–650 (2023). doi: 10.1038/s41586-023-06362-4; pmid: 37437602
98. T. Plum *et al*., Mast cells link immune sensing to antigen-avoidance behaviour. *Nature* **620**, 634–642 (2023). doi: 10.1038/s41586-023-06188-0; pmid: 37438525
99. E. Kiner *et al*., Gut CD4$^+$ T cell phenotypes are a continuum molded by microbes, not by T_H archetypes. *Nat. Immunol.* **22**, 216–228 (2021). doi: 10.1038/s41590-020-00836-7; pmid: 33462454
100. A. Butler, P. Hoffman, P. Smibert, E. Papalexi, R. Satija, Integrating single-cell transcriptomic data across different conditions, technologies, and species. *Nat. Biotechnol.* **36**, 411–420 (2018). doi: 10.1038/nbt.4096; pmid: 29608179

ACKNOWLEDGMENTS

We thank D. Littman, V. Gradinaru, M. Wu, M. Rao, A. Rudensky, and members of the Chiu and CBDM labs for insightful discussion and advice; L. Yang and D. Mallah for help with computational analyses; K. Hattori and S. Choi for help with mice; P. Montero-Llopis and the MicRoN facility for microscopy; Boston Children's Hospital Viral Core for virus stocks; and I. Magill for single-cell sequencing. **Funding:** This work was supported by National Institutes of Health (NIH) grants AI125603 and AI150686 to C.B. and D.M.; the JPB Foundation (C.B. and D.M.); the Food Allergy Science Initiative (S.D.L. and I.M.C.); NIH grant RO1DK127257 to I.M.C.; and the Kenneth Rainin Foundation (I.M.C.). K.A.M. was supported by NIH grant F32DK137456, and S.G.-P. was supported by a fellowship from the European Molecular Biology Organization (ALTF 547-2019). **Author contributions:** Y.Z., K.A.M., I.M.C., and C.B. conceptualized the study; Y.Z., K.A.M., S.G.-P., N.-R.B., D.Y., H.B., S.D.L., R.K., and A.S. performed experiments and analyzed data; C.B., D.M., and I.M.C. provided funding; Y.Z., K.A.M., I.M.C., and C.B. drafted the manuscript; and all authors reviewed and edited the manuscript. **Competing interests:** S.D.L. was a consultant for Kallyope, Inc. I.M.C. consults for GSK Pharmaceuticals, and his lab has received sponsored research from Moderna and AbbVie/Allergan. The other authors declare that they have no competing interests. **Data and materials availability:** All data needed to evaluate the conclusions in the paper are present in the paper or the supplementary materials. Data that are newly reported in this paper are available at the National Center for Biotechnology Information (NCBI) Gene Expression Omnibus (GEO) and Sequence Read Archive (SRA) repositories under accession nos. GSE240982 and GSE267709.

SUPPLEMENTARY MATERIALS

science.org/doi/10.1126/science.adk1679
Figs. S1 to S10
MDAR Reproducibility Checklist
Data S1 to S7

Submitted 18 August 2023; resubmitted 21 March 2024
Accepted 3 June 2024
10.1126/science.adk1679